Mastering the synergy between $Na_3V_2(PO_4)_2F_3$ electrode and electrolyte: A must for Na-ion cells

Parth Desai,[1,2,3] Juan Forero-Saboya,[1] Valentin Meunier,[1,2,3] Gwenaëlle Rousse,[1,2,3] Michael Deschamps,[3,4] Artem M. Abakumov,[5] Jean-Marie Tarascon*,[1,2,3] and Sathiya Mariyappan**,[1,3]

[1]Chimie du solide et de l'énergie (CSE), UMR 8260, Collège de France, 75231 Paris Cedex 05, France
[2]Sorbonne Université, 4 Place Jussieu, 75005, Paris, France
[3]Réseau sur le Stockage Electrochimique de l'Energie (RS2E), FR CNRS 3459, France
[4]CNRS, CEMHTI UPR3079, Université d'Orléans, 1D avenue de la recherche scientifique, 45071 Orléans Cedex 2, France
[5]Center for Energy Science and Technology, Skolkovo Institute of Science and Technology, 3 Nobel Street, Moscow, 121205, Russia
*Correspondence: jean-marie.tarascon@college-de-france.fr

**Correspondence: sathiya.mariyappan@college-de-france.fr

Abstract:

Sodium-ion batteries are emerging as suitable energy storage devices for special applications such as high-power devices with the advantages of being cheaper and more sustainable than the Li-ion equivalents. The sodium ion cells consisting of polyanionic $Na_3V_2(PO_4)_2F_3$ - hard carbon electrodes exhibit high power rate capabilities but limited cycle life, especially at high temperatures. To circumvent this drawback we herein conducted in-depth analyses of the origins of structural degradations occurring in $Na_3V_2(PO_4)_2F_3$ electrodes upon long cycling. Vanadium dissolution with associated parasitic reactions is identified as one of the major reasons for cell failure. Its amount varies depending on the electrolyte, with NaTFSI-based electrolyte showing the least vanadium dissolution as the $TFSI^-$ anion decomposes without producing acidic impurities, in contrast to the Na-PF_6-based electrolyte. The dissolved vanadium species undergoes oxidation and reduction processes at the $Na_3V_2(PO_4)_2F_3$ and HC electrodes, respectively, with the electrochemical signature of these processes being used as a fingerprint to identify state of health of the 18650 cells. Having found that surface reactivity is the primary cause of vanadium dissolution we provide methods to mitigate it by combining surface coating and optimized electrolyte formulation.

Key words: Na-ion batteries, transition metal dissolution, hard carbon poisoning, surface coating, high temperature cycling

Broader context

The huge success of lithium-ion batteries in the last decades has fueled the boom of portable electronics and has paved the way for the energy transition from fossil fuels to more renewable energy sources. However, a full decarbonization will require the development of complementary energy storage technologies relying on more sustainable and more abundant raw materials. Among the different next-generation batteries being explored, sodium-ion is the most mature, given the easy technology transfer from the existing Li-ion processes. Indeed, the commercialization of Na-ion cells is imminent, with several companies worldwide showing a growing interest in their development and optimization. In such thriving research ecosystem, studying the cell degradation is crucial as its understanding will allow the development of long-cycle life cells. In this study we tackle the problem of transition metal dissolution pertaining to the promising sodium-ion technology ($Na_2V_2(PO_4)_2F_3$-hard carbon), that can either result in cell degradation and eventually cell dead. We show that this issue can be cured by combining the specific design of electrolytes together with coating approaches, hence enhancing the high temperature performances of the NVPF-HC technology that is a must to reach a highly demanding energy market.

Introduction:

Even though lithium-ion batteries (LIBs) have achieved unprecedented commercial success in the previous decades, uneven distribution and poor abundance of lithium lead to raw material supply tensions that pose a severe challenge for their use in large-scale applications.[1,2] In this regard, sodium-ion batteries (NIB) are an attractive complementary technology that shares a similar working principle and cell engineering to LIBs.[3,4] Sodium has numerous advantages over Li in terms of abundance (~23,000 ppm vs. 20 ppm in the earth's crust), distribution, and cost, offering economic sustainability.[5] However, one of the significant drawbacks of NIBs is their lower energy density than LIBs. In turn, sodium ion chemistries such as $Na_3V_2(PO_4)_2F_3$ (NVPF)- hard carbon (HC) and Prussian blue analogs (PBA)- hard carbon offer high-power capabilities making them more attractive and cheaper alternatives for high-power applications[6–10] such as hybrid grid storage, power tools, fast (dis)charging electromotive, military equipment, etc.

In this context, our group in collaboration with the Na-ion battery start-up 'TIAMAT Energy (France)' is actively working to develop high-power NVPF – HC based Na-ion cells. NVPF is a structurally robust material, which usually shows a reversible capacity of ~120 mAh/g (Supporting Fig. S1) and exhibits excellent cycling performance at ambient temperature.[11–13] The NVPF voltage profile displays two distinct steps (Supporting Fig. S1) at 3.7 V and 4.2 V, corresponding to the subsequent (de)insertion of two sodium ions from one formula unit. This high redox potential of 4.2 V vs. Na^+/Na^0 (or equivalent to 4.53 V vs. Li^+/Li^0) creates severe issues of electrolyte oxidation that could further trigger parasitic reactions, especially at a high temperature of 55 °C.[6,8] We have previously shown that one way to alleviate this issue involves stabilizing the electrolyte against oxidation or reduction via several additives.[8,14–16] For instance, by adding vinylene carbonate, sodium oxalatodifluoroborate, succinonitrile, and tri-methyl silyl phosphite (VC + NaODFB+ SN + TMSPi) to the control (1M $NaPF_6$ in EC+PC+DMC) electrolyte,[8,16] we could drastically reduce but not fully eliminate the capacity loss at 55 °C. Thus, improving further the high-temperature

cyclability of NVPF-HC cells without losing their high-power capability, calls for a greater understanding of the aging mechanism of NVPF-HC cells at both high and ambient temperatures.

Learning from the Li-ion battery technology, another source of cell degradation besides electrolyte oxidation is rooted in the transition metal (TM) dissolution as exemplified with the $LiMn_2O_4$/Graphite chemistry, whose practical aspect has long been plagued by Mn dissolution.[17–20] Dissolution-migration of TM from the positive electrode and its deposition on the negative electrode is considered as the cause of capacity fade.[21,22] Moreover, such a TM dissolution is not specific to the Li-ion chemistry as it was recently reported for Na-based positive electrodes such as sodium layered oxides.[23–26] Thus, we decided to study the V-dissolution thoroughly in NVPF-HC cells depending on the electrolyte formulation (solvent and salt), temperature, and state of charge (SOC) of the NVPF material.

From post-mortem analyses of the NVPF-HC cycled cell, we find that the positive electrode suffers from vanadium dissolution that in turn poisons the electrolyte and the HC negative electrode. Further digging into the origin of this dissolution issue, we thus study its dependence on both electrolyte decomposition and structural evolution upon cycling. Using combined TEM, NMR, and IR analyses, together with electrochemical analyses of the different electrolyte/solvent leached samples, we observe a strong influence of the electrolyte formulation on V-dissolution that triggers structural changes in the NVPF material. Subsequently, by carrying out electrochemical analyses on the vanadium-containing electrolyte, we identify, besides the structural aspects, the reactivity of dissolved vanadium in both positive and negative electrode surfaces that led to further cell deterioration. Finally, we provide evidence that such effects can be cured by the use of well-designed carbon coatings together with optimized electrolyte formulation.

Experimental Section:

Cell assembly and electrochemical tests: The $Na_3V_2(PO_4)_2F_3$ (NVPF) sample containing ~5% carbon coating is used throughout the studies except for studies on 18650 cells where the NVPF containing either 3 - 7% carbon coating were used. The NVPF and HC electrodes coated (one side) on Al foil for coin cell experiments as well as the dry 18650 cells without electrolyte for prototype cell assembly were received from TIAMAT, Amiens. The electrochemical tests on $Na_3V_2(PO_4)_2F_3$ (NVPF) were carried out in either Na-metal half-cell using Na metal as a counter (negative) electrode, or Na-ion full cell where hard carbon casted on aluminum foil was used as the negative electrode. Either 2032 coin type cells or 18650 cylindrical type cells (exclusively for full cell analyses) were used for the study. The electrolyte used is 1M $NaPF_6$ in Ethylene carbonate (EC)-Propylene carbonate (PC) – Dimethyl Carbonate (DMC) in 1:1:2 volume ratio, with or without electrolyte additives. The electrolyte additives used are 3 wt. % succinonitrile (SN), 1 wt. % vinylene carbonate (VC), 0.5 wt. % sodium oxalatodifluoroborate (NaODFB) and 0.5 wt.% tri-methylsilylphosphite (TMSPi). A mixture of 0.7M $NaPF_6$+ 0.3M NaTFSI is used as an electrolyte salt for some selected experiments.

Coin cell assembly was carried out in an argon-filled glove box using a glass fiber separator, whereas 18650 cells were filled with electrolyte and sealed in a dry room. For analyzing the electrochemical performance of the $Na_1V_2(PO_4)_2F_3$ samples after treatment with different electrolytes, Na-metal half cells were assembled with 1M $NaPF_6$ in PC as electrolyte. Three-electrode cyclic voltammetry tests were performed with glassy carbon as the working electrode, Pt wire as the counter electrode, and Ag/Ag^+ organic reference electrode (calibrated against Na metal). Leached electrolyte for cyclic voltammetry (CV) was recovered as explained in the leaching procedure section next or by washing the NVPF recovered from 18650 after current interruption device (CID) break (mentioned as ‘green electrolyte’ as the prepared electrolyte was greenish due to the presence of dissolved vanadium in it).

All electrochemical measurements were carried out using a Biologic battery cycler/potentistat-galvanostat, at a specific cycling rate and temperature as specified in the main text.

Leaching procedure: Firstly, 300 mg of $Na_3V_2(PO_4)_2F_3$ powder (90% active mass-10% carbon black Super P) was charged in a homemade big cell to the $Na_1V_2(PO_4)_2F_3$ composition using 1M $NaPF_6$ in PC electrolyte. The powder was recovered from the cell and washed several times with DMC before drying in the glovebox antechamber. For leaching, either a solvent mixture (EC – PC-DMC) or the electrolytes containing 1M salt from $NaPF_6$, $NaClO_4$, $NaBF_4$, NaFSI, and NaTFSI in EC-PC-DMC (1:1:1 by volume) were used. All the salts were dried overnight in a Büchi oven under vacuum at 80 °C before transferring into the glove box. All the solvents were dried over molecular sieves till the water content of less than 10 ppm, as measured by Karl-Fischer titration. Secondly, the electrolyte or solvent (3 mL) was mixed with $Na_1V_2(PO_4)_2F_3$ (20 mg) in a 15 mL polypropylene vial and sealed in an aluminum bag inside an argon-filled glovebox. The aluminum bag was then transferred to a 55 °C oven for 21 days of leaching. After leaching, the Al bags were transferred to an argon-filled glovebox, and the samples were recovered. The leached NVPF powder was separated from the electrolyte by centrifugation and washed several times with DMC before drying under vacuum. The recovered electrolyte was filtered using a 0.2 μm polypropylene syringe filter (VWR international) to ensure the removal of any NVPF particles in the recovered electrolyte for analyses. The separated solid (leached NVPF) and the liquid (leached electrolyte) were used for further characterization.

Quantifying vanadium dissolution using ICP-MS: For the 2032 coin cell mode, HC electrodes and the separator touching the HC electrodes were recovered after the specified charging/storage procedure. HC + separator was digested in 10.000 mL of 2 wt. % nitric acid (Suprapur, 65 % HNO_3, Merck, vanadium content ≤ 0.5 ppb), and solutions were sonicated and rested overnight. Solutions were filtered with polypropylene 0.2 μm PP syringe filters and diluted with 2 wt. % nitric acid solution until final vanadium concentrations between 1 ppb to 1 ppm were reached. The vanadium

amount was quantified using inductively coupled plasma mass spectroscopy (ICP-MS, Nexion 2000, Perkin Elmer). The calibration was obtained from three diluted vanadium standard solutions (TraceCERT, 1 $mg.L^{-1}$ V in nitric acid, Sigma-Aldrich). For the leached electrolyte obtained in the leaching procedure section, the 200.00 μL of electrolyte was diluted until final vanadium concentrations between 1 ppb and 1 ppm were obtained and measured with ICP-MS.

X-ray diffraction (XRD): Synchrotron XRD patterns (λ = 0.4589 Å) were collected via the mail-in service of the 11-BM beamline at the Advanced Photon Source at Argonne National Laboratory. The leached and reference NVPF powders were sealed in glass capillaries and kept inside the kapton holder. The Rietveld refinement of the synchrotron XRD pattern (for solvent leached NVPF) was performed using the FullProf program.[27] *Operando* X-ray measurements were taken by a BRUKER D8 Advance diffractometer with Cu Kα radiation ($\lambda K\alpha_1$ = 1.54056 Å, $\lambda K\alpha_2$ = 1.54439 Å) and a Lynxeye XE 583 detector. The *operando* XRD analyses were conducted using a homemade airtight XRD cell equipped with a beryllium window.

Transmission electron microscopy (TEM): Samples for transmission electron microscopy (TEM) were prepared in an Ar-filled glove box by grinding the leached NVPF powder in an agate mortar in dimethyl carbonate and depositing drops of suspension onto a copper TEM grid with a holey carbon support layer. The sample was transported to the TEM column with a Gatan vacuum transfer holder avoiding contact with air and moisture. High angle annular dark field scanning transmission electron microscopy (HAADF-STEM) images, energy-dispersive X-ray (EDX) spectra, STEM-EDX maps, electron energy loss spectra (EELS) and STEM-EELS maps were collected with a probe-corrected Titan Themis Z electron microscope operated at 200 kV equipped with a Super-X EDX detector and a Gatan Quantum ER965 spectrometer. The energy resolution, measured from the full width at half maximum of the zero-loss peak, was 0.175 eV.

Scanning Electron Microscopy (SEM): SEM images of the NVPF with different carbon coating were obtained on an FEI Magellan scanning electron microscope equipped with an Oxford Instruments energy dispersive X-ray spectroscopy (EDX) detector. EDX analyses of the NVPF particles were carried out using an acceleration voltage of 20 kV.

Fourier-Transform Infrared (FTIR) Spectroscopy: The leached NVPF powders were discharged to 2 V (0% state of charge) vs. Na metal for FTIR measurement. FTIR spectra were recorded on a Nicolet iS5 FTIR spectrometer, mounted with a diamond Attenuated Total Reflectance accessory (iD1 ATR). All the spectra were taken using 16 scans with a 4 cm^{-1} resolution from 2000 to 400 cm^{-1}. The background correction is performed by measuring the ambient atmosphere under the same conditions as for the leached NVPF.

Mass Spectroscopy (MS): Mass spectra were recorded for the gas inside the pouch bags collected during the leaching process of Na_1VPF with NaTFSI or $NaPF_6$ for 21 days at 55 °C. The pouch bags with samples containing polypropylene tubes were bulged up due to gassing after 21 days of storage at 55 °C. A needle was pierced to the pouch and the gas was transported to the mass spectrometer via a gastight syringe. The gas samples were then injected into an ExQ gas analysis system (Hiden Analytical, USA) composed of a HAL (Hiden Analytical) series quadrupole mass spectrometer, an ultra-high vacuum (UHV) mass spectrometer vacuum chamber, a vacuum pumping system and a QIC series capillary inlet. The partial pressures are eventually determined for each gas based on their mass to charge ratio (m/z), after ionization in the ionization source of the MS.

Nuclear magnetic resonance (NMR) spectroscopy: The leached NVPF powders were discharged to 2 V (0% state of charge) vs Na metal for solid state NMR analyses. Solid-state ^{31}P and ^{23}Na NMR spectra were recorded on electrode materials with a 4.7 T (200 MHz for ^{1}H) Bruker WB spectrometer equiped with an Avance HD console and a 1.3 mm Magic Angle Spinning (MAS) double resonance ^{1}H-^{19}F/^{31}P-^{15}N probe. The rotors were filled inside an argon filled glovebox and

the rotor were spinning at ν_R = 60 kHz under 100% N_2 atmosphere. The solid-state NMR spectra were recorded with a rotor synchronized Hahn echo sequence (90° – $1/\nu_R$ – 180°- $1/\nu_R$ – acquisition), and the chemical shift were referenced with 85% H_3PO_4 in water for ^{31}P and 1 M NaCl in water for ^{23}Na, both at 0 ppm. Full relaxation of the magnetization was achieved with a 50 ms recovery delay between each transient in both case. 1 024 000 transients were recorded for ^{31}P and 10240 for ^{23}Na.

Liquid-state spectra were recorded in the same spectrometer with a double resonance probe equiped with 10 mm inserts, tuned to ^{31}P or ^{51}V. Liquid-state spectra were recorded for all samples inside 5 mm glass tubes filled in the glove box, and sealed with parafilm. An N_2 flow of 500 L/h was sent inside the probe to shield the sample from the air. The spectra were recorded with a 90°-acquisition sequence. 102 400 transients were recorded for ^{31}P (recovery delay 5s) and 1 024 000 transients were recorded for ^{51}V (recovery delay 50 ms).

The presence of HF in the electrolyte was evaluated by ^{19}F liquid-state NMR spectra, recorded in a Bruker 7.046 T (282 MHz for ^{19}F) Advance III NMR spectrometer mounted with a 5 mm HX(F) probehead. The samples were meassured in a 5 mm glass tube equiped with a D_2O-filled inset for signal lock. The spectra were recorded with a 90° adquisition sequence, over 16 scans (5 s adquisition time each) and 10 s recovery delay, and were referenced with the expected signal of the anion (PF_6^- or $TFSI^-$ accordingly).

Results and Discussion:

Post-mortem analysis of NVPF-HC cells to understand the degradation mechanism:

Dry 18650 NVPF-HC cells were received from TIAMAT and filled with 1M $NaPF_6$ in EC-PC-DMC (1:1:1 by volume) electrolyte. The cell formation and cycling were performed at 55 °C using a cycling rate of C/5 (1C= 128 mAh/g). Fig. 1a shows the capacity retention plot, with 93 % of the original capacity retained after 28 cycles. Although the cell does not show a big capacity loss, the current interruption device (CID) broke after ~10 days (28 cycles) at 55 °C, which is indicative of a

huge pressure increase (~ 15 bars) inside the cell due to parasitic reactions enlisting gaseous by-products generation.

After the CID break, the cell was opened and individual electrodes were recovered for analysis. Upon washing with EC-PC-DMC, the NVPF electrode releases some yellow/ slight green coloration into the solvent (Fig. 1b), that indicates the dissolution of some vanadium as confirmed by inductively coupled plasma-mass spectroscopy (ICP-MS). This suggests the presence of easily soluble vanadium species in the NVPF electrode, contrary to the pristine NVPF electrode, which shows no dissolution in this solvent mixture. Additionally, by SEM-EDX analysis, we spotted (Fig. 1c) the presence of deposited vanadium on the recovered HC electrode surface as well. Altogether, these results unambiguously indicate the presence of V-dissolution in the cycled NVPF/HC cell, with part of the soluble vanadium species going into the electrolyte that further deposits to hard carbon negative electrode.

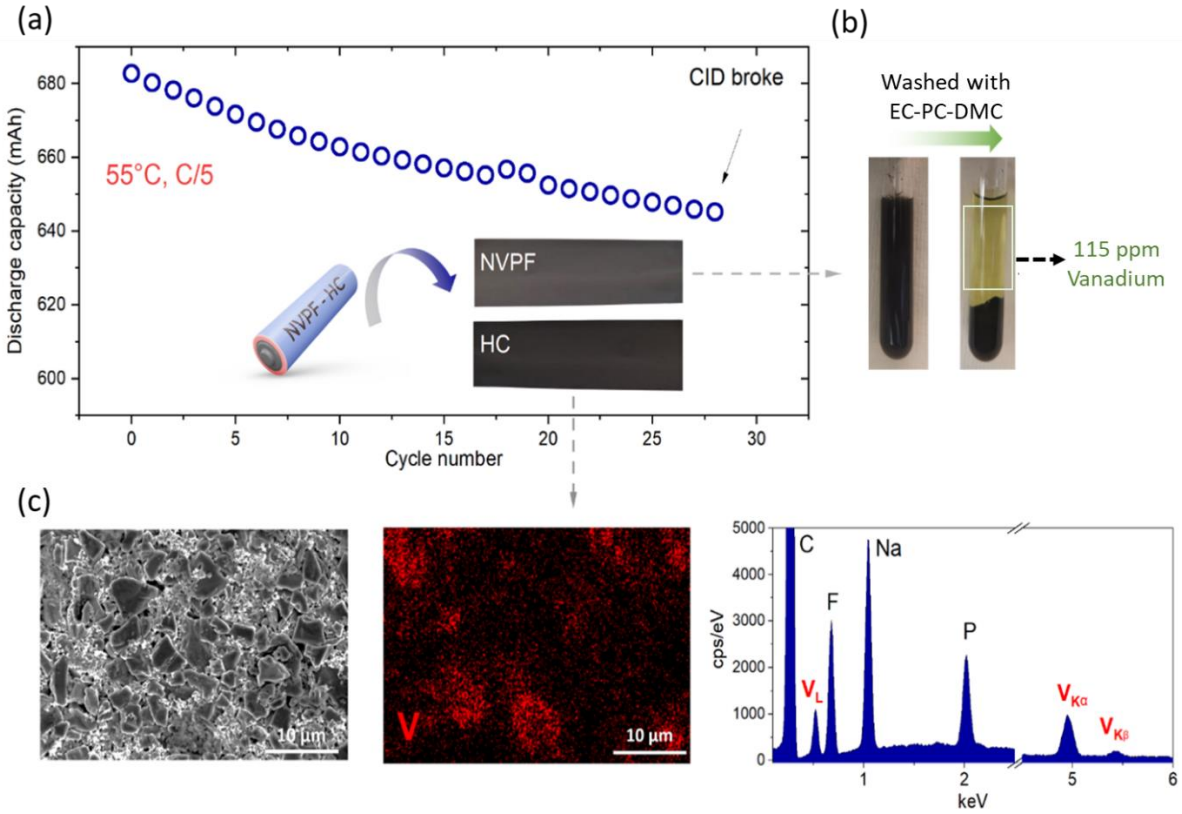

Fig. 1: **Electrochemical characterization and post-mortem analysis of cylindrical 18650-type NVPF|HC cell cycled with C/5 rate at 55 °C.** (**a)** Discharge capacity retention plot of NVPF and HC cell cycled at 55 °C. The data from formation cycles are not included here for clarity purpose. The inset shows the NVPF and HC electrodes recovered after the CID break. (**b)** Green/yellow colored solution recovered by washing 360 mg of cycled NVPF electrode with 3 mL of EC-PC-DMC; ICP results showed 115 ppm dissolved vanadium in this solution. (**c)** SEM/EDX analysis of recovered HC with SEM image (left), EDX elemental mapping of vanadium (middle) and EDX spectra (right).

Quantification of vanadium dissolution:

In order to quantify the amount of vanadium dissolved at different cycling conditions, a series of experiments were performed in coin cells employing fresh electrodes (single side casted NVPF and HC electrodes on Al foil), two glass fiber separators soaked in 1M $NaPF_6$ in EC-PC-DMC electrolyte. The cells were cycled to a particular state of charge (SOC), and maintained at that potential for 24 hrs. or 1 week prior being disassembled. The experiments were done either at 25°C or 55°C.

The hard carbon electrode together with one separator next to HC, were recovered from the cells and digested separately or together using 2% HNO_3. Worth mentioning that, we have not used the separator next to the NVPF because of some remaining attached NVPF particles that would have rendered our measurements meaningless. The obtained solutions were filtered and analyzed by ICP-MS for vanadium content with the corresponding detected amounts indicated in Fig. 2a. Note that the mathematical sum of the vanadium detected from the carbon electrode (~0.1 %) and separator (~0.44 %) alone is nearly equal to the experimental value obtained (~0.6 %) by analyzing both at the same time, hence explaining why from now on we solely report the total amount of vanadium in both HC+ separator at once for meaningful comparisons. Following this protocol, we show (Fig. 2b) that the V-dissolution increases with increasing oxidation potential/state of charge of the NVPF electrode, with maximum dissolution observed for 100% state of charge (4.3 V). Further, increasing either the resting period at high potential or the cycling temperature promotes V-dissolution (Fig. 2c).

Moreover, Fig. 2d shows that the amount of dissolved vanadium keeps increasing upon cycling, however, at a lower speed with increasing cycle numbers.

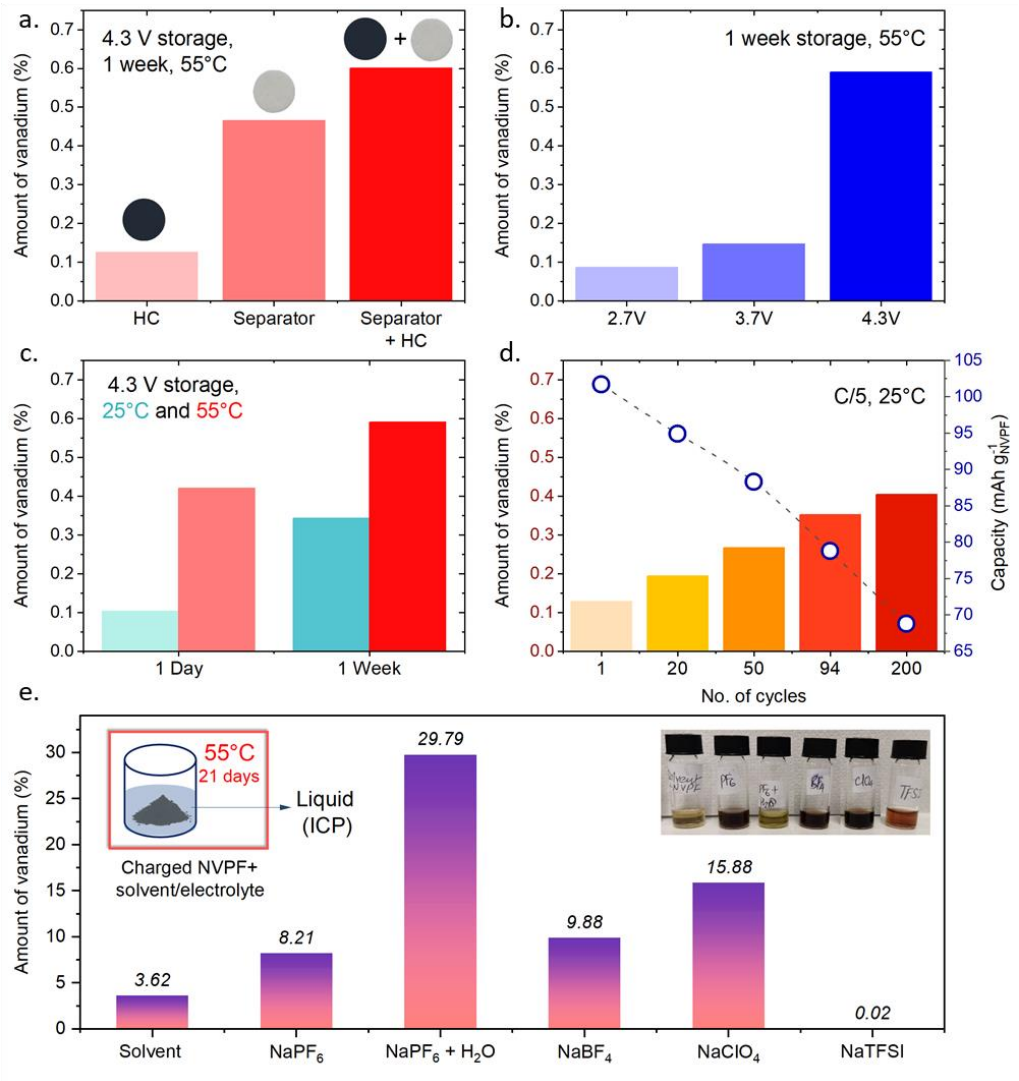

Fig. 2: **Different factors affecting vanadium dissolution.** The amount of vanadium dissolved from NVPF detected by ICP-MS. For better comparison, the obtained ppm values are converted to %V where the dissolved vanadium is normalized with respect to total vanadium present in the NVPF electrode taken for the experiment. The %V detected from (**a)** Hard carbon electrode, separator separately and hard carbon + separator together recovered from NVPF-HC coin cells stored for 1 week at 4.3 V and 55 °C. (**b)** Hard carbon+ separator recovered from cells cycled to different upper cutoff voltages of 2.7 V, 3.7 V and 4.3 V and stored for 1 week at 55°C. (**c)** HC+ separator recovered from cells charged to 4.3 V and stored at 25°C and 55°C for 1 day and 1 week. (**d)** Amount of dissolved vanadium and discharge capacity vs. cycle number for NVPF-HC coin cells cycled at 25 °C. In all the experiments from a-d, the electrolyte used is

1M $NaPF_6$ in EC-PC-DMC. (**e)** Amount of vanadium dissolved from the charged NVPF (4.3 V, $Na_1V_2(PO_4)_2F_3$) powder leached in EC-PC-DMC without (solvents alone) or with different Na-salts at 55 °C for 21 days.

At this stage, a legitimate question regards whether such V-dissolution is limited to $NaPF_6$ based electrolytes? To address this point, we next studied the effect of different electrolyte formulations by solely changing the nature of the salt and not the solvent. The experiments were done by placing the fully charged NVPF powders (4.3 V vs. Na, having the $Na_1V_2(PO_4)_2F_3$ composition) in the presence of the studied electrolytes and stored at 55 °C for 21 days (see Supporting Fig. S2). After this period, the supernatant liquid and solid products were separated by centrifugation and filtration. The liquid supernatants were analyzed via ICP-MS for their vanadium content and the solids were analyzed by XRD to eventually spot the structural evolutions. From now on, the charged material leached with EC-PC-DMC solvents (with no salt) is named as SL-NVPF (Solvent Leached-NVPF), whereas those leached with electrolyte bearing salts are referred using the salt anion, so that the sample leached with $NaPF_6$ is denoted as PF_6-NVPF (and so on TFSI-NVPF, ClO_4-NVPF, etc.).

The amounts of dissolved vanadium are shown in Fig. 2e and as expected, this amount is the largest with the electrolyte containing 200 ppm of water, since water is known to trigger the hydrolysis of PF_6^- with the liberation of HF that causes copious active material dissolution, similar to what has been reported for $LiFePO_4$ and $LiMn_2O_4$.[19,28–31] A lower but significant amount of dissolved vanadium was observed in other electrolytes, following the order of $NaPF_6$+H_2O > $NaClO_4$ > $NaBF_4$ > $NaPF_6$ > solvent > NaTFSI. Interestingly, the NaTFSI-based electrolyte, with the lower tendency for HF formation[32–34], exhibits the least (almost nil) V-dissolution from 'charged NVPF'. Note that similar results (almost no V-dissolution) were obtained with NaFSI-based electrolyte as well (supporting Fig. S3). The results suggest that the formation of acidic by-products from electrolyte oxidation might be behind the observed V-dissolution sequence, however, it is not the only cause as $NaClO_4$ and $NaBF_4$ electrolytes that are known to generate less acidic species showed more V-dissolution than $NaPF_6$ electrolyte[35–37]. This suggests that the salt anion or its oxidized by-products

most likely play a role in the V-dissolution. Lastly and surprisingly, we found that a pure solvent mixture (EC- PC- DMC) also leads to some V-dissolution, although it cannot be explained either by the presence of any acidic impurity or oxidized salt anion species. This suggests a copious reactivity of oxidized NVPF material with the carbonate solvent itself, causing some vanadium losses, further complexing the V-dissolution mechanism.

Overall, we have observed that a significant amount of vanadium is dissolved from the NVPF material into the electrolyte, particularly when it is fully charged ($Na_1V_2(PO_4)_2F_3$). In the following sections we will explore the effect of this dissolution on the NVPF material, and on the general aging of the NVPF | HC cells upon cycling.

Structural evolutions of NVPF due to vanadium dissolution:

To interrogate the effect of V-dissolution on the material's electrochemical performances, Na-NVPF half cells were assembled using the leached NVPF materials as positive electrodes and 1M $NaPF_6$ in PC as electrolyte and the cells were cycled by starting on oxidation (Fig. 3a). For comparison purpose, the as-charged $Na_1V_2(PO_4)_2F_3$ material that is stored in the argon atmosphere without any treatment with solvent/electrolyte is also analyzed. Asides from the cell based on the as-charged NVPF (no leaching), all the other cells have a starting potential (OCV) falling within the low voltage plateau (< 3.9 V), implying the uptake of Na during the leaching process, with this effect being more pronounced with NaTFSI. Note that solvent-treated NVPF (SL-NVPF), where there is no extra sodium for uptake in the EC-PC-DMC blend, also showed some oxidation in the first charge.

In the subsequent cycle, charge and discharge curves (Fig. 3b) show each stair-case profiles reminiscent of NVPF, although it is relatively less pronounced for the SL-NVPF with a profile being nearly alike that of oxygen substituted NVPF phase (Supporting Fig. S4).[38] Moreover, except for the SL-NVPF, PF_6-H_2O-NVPF, and TFSI-NVPF specimens, the measured reversible capacity is lower than the usual capacity of NVPF (~120 mAh/g), implying that the leaching process is associated with

V-dissolution (leading for example to $NaV_{2-x}\square_x(PO_4)_2F_3$) or to structural deterioration of NVPF. The latter is evidenced by the fact that the observed loss in capacity (Fig. 3b) does not correlate with the calculated capacity loss if we would simply remove vanadium during leaching (Supporting Fig. S5). Therefore, NVPF is decomposing into one electrochemically active and another inactive phase(s) with the latter being responsible for the electrochemical dead weight and reduced capacity.

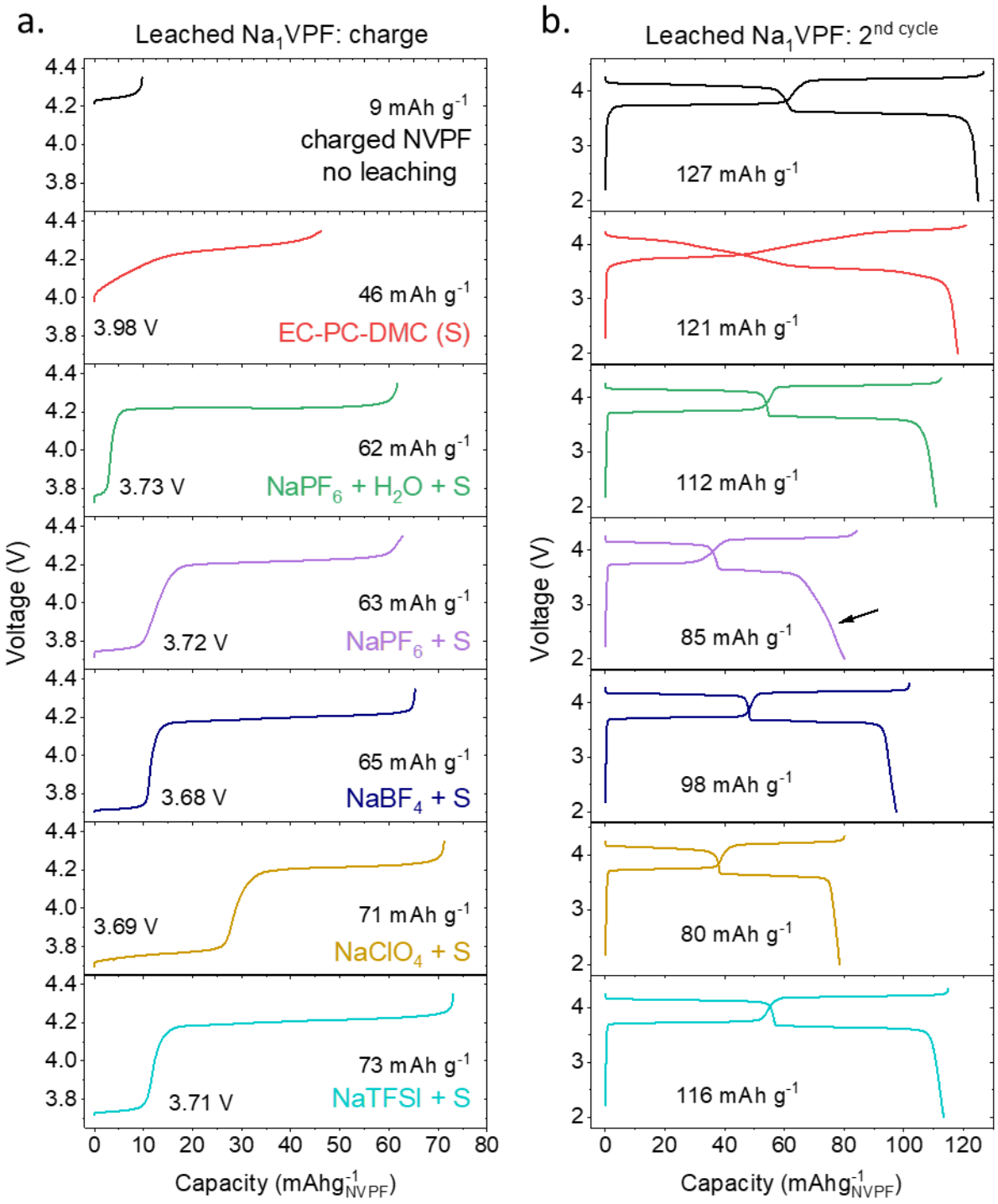

Fig. 3: **Electrochemical performance of leached/ unleached Na_1VPF in Na-half cells: (a)** First charging curve. The OCV after the cell assembly and observed charge capacity is mentioned in figure. **(b)** The second cycle. All leaching experiments were carried out at 55 °C for 21 days in the mentioned electrolyte or solvents. The salt used is mentioned in the Fig. 3a and 'S' represents solvents mixture EC-PC-DMC.

From the open circuit voltage of the leached samples in Fig. 3a, one could hypothesize that the structure should consist of a mixture of $Na_2V_2(PO_4)_2F_3$ and $Na_{2+x}V_2(PO_4)_2F_3$ phases. To check this hypothesis, synchrotron XRDs were collected for all the leached samples and compared with the patterns of $Na_1V_2(PO_4)_2F_3$, $Na_2V_2(PO_4)_2F_3$ and $Na_3V_2(PO_4)_2F_3$ in Fig. 4a and supporting Fig. S6. For the sake of clarity, we solely plot the 2θ=[4.6-8.5°] region which is very sensitive to the sodium-vacancy ordering and Na content (x).[13,39] Interestingly, the PF_6-H_2O-NVPF sample looks single phase with an XRD pattern alike $Na_2V_2(PO_4)_2F_3$ (Fig. 4a). However, both are slightly different from the previously reported XRD pattern for $Na_2V_2(PO_4)_2F_3$, which was indexed in the *I* 4/*m m m* space group with *a*≈6.30 Å and *c*≈10.81 Å by Bianchini et al[39]. Our synchrotron patterns for the PF_6-H_2O-NVPF sample and for $Na_2V_2(PO_4)_2F_3$ cannot be indexed using this tetragonal cell, as the (2 0 0) peak is split into two peaks at 2θ ≈ 8.335°, so that we engaged into the structural resolution of this phase. The pattern of the PF_6-H_2O-NVPF sample can be indexed using a body-centered orthorhombic unit cell with space group *I m m m* and lattice parameters *a* = 6.311646(6) Å, *b* = 6.318539(6) Å and *c* = 10.817618(11) Å, which is a distortion of the tetragonal *I* 4/*m m m* cell. The Rietveld refinement of PF_6-H_2O-NVPF is shown in Fig. 4b, and the Na content was refined to 0.489(12) leading to a $Na_2V_2(PO_4)_2F_3$ composition (the refined structural parameters are given in Supporting Information, Table S1). This phase is denoted 'P' hereafter and dotted lines are used to highlight its main Bragg peaks in Fig. 4a.

The phase 'P' together with another 'A' phase is present in the BF_4-, TFSI-, and PF_6-NVPF samples. In contrast, this P phase is not present for the ClO_4-NVPF sample at the expense of the 'B' and 'C' phases that became the majority. By comparing with the *operando* XRD of NVPF (Supporting Fig. S7), the 'A' and 'B' phases could be closely matched to $Na_{\sim 2.2}V_2(PO_4)_2F_3$ with

slightly differing sodium stoichiometry and 'C' phase with $Na_{\sim 3}V_2(PO_4)_2F_3$. As a result, the major peaks in all the electrolyte leached samples could be indexed with NVPF structure with difference in sodium content. Moreover, worth mentioning that Rietveld refinement attempts for the collected XRD pattern of SL-NVPF fails as the peaks are too broad, indicative of structural disorder driven by the leaching process.

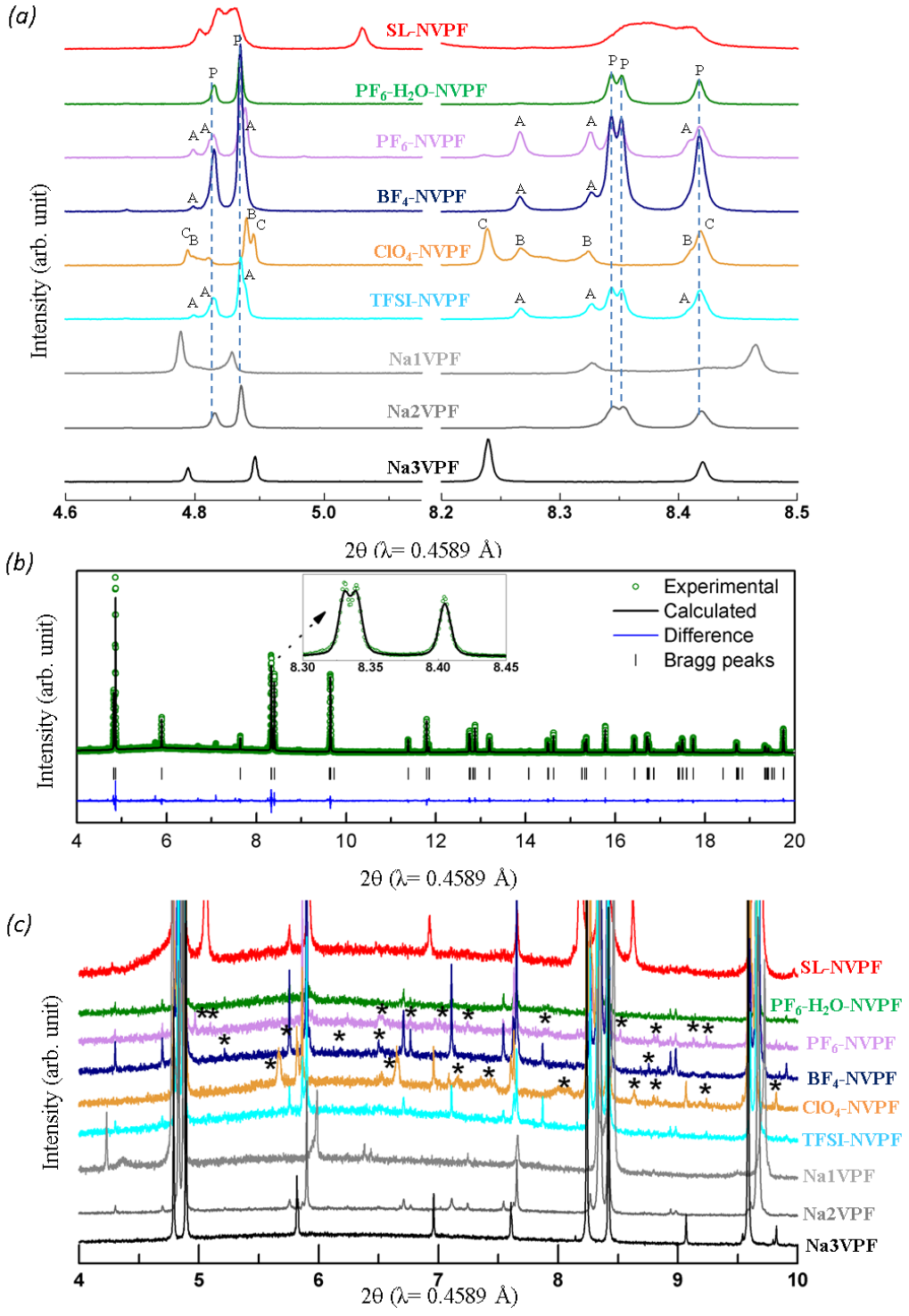

Fig. 4: **X-ray diffraction pattern of leached Na_1VPF. (a)** The 11BM synchrotron powder XRD pattern of the recovered Na_1VPF powder after leaching treatment in the mentioned electrolyte at 55 °C for 21 days. For the comparison, synchrotron patterns of unleached $Na_1V_2(PO_4)_2F_3$, $Na_2V_2(PO_4)_2F_3$ and $Na_3V_2(PO_4)_2F_3$ are also presented. (b) Rietveld refinement of the PF_6-H_2O-NVPF sample where the experimental, calculated and difference patterns are marked by green circle points, black line and blue line, respectively. The vertical tick marks correspond to Bragg reflections in the *I m m m* orthorhombic cell (see text) (c) Zoomed (in y-axis) image of Fig. 4a showing the extra peaks that are not indexed by NVPF structure and must be due to the decomposed products of NVPF during the leaching process.

By zooming in the XRD patterns of Fig. 4a (see Fig. 4c) we observe for most of the leached samples, with the exception of the PF_6-H_2O- and TFSI-NVPF ones, some extra peaks that could not be indexed with NVPF structure. These extra peaks may correspond to the electrochemically inactive phases we observe during cycling, which act as dead weight reducing the observed capacity of the material, as mentioned previously. The absence of extra peaks for the PF_6-H_2O-NVPF through the leaching process does come as a surprise since H_2O in presence of PF_6^- leads to the formation of HF, which would provoke partial dissolution. However, absence of these extra peaks suggests that the formed HF is dissolving such inactive phases, leaving behind only the electroactive NVPF material. This is corroborated by the observed capacity of the PF_6-H_2O-NVPF matching closely the expected for NVPF.

Lastly, it looks like this Na uptake reaction is the only one occurring for the TFSI-NVPF as it is structurally unaffected with almost no capacity loss (in Fig. 3b). Altogether, the XRD and cycling results show that all the leached samples self-discharged via an uptake of Na ions. With the exception of SL-NVPF, all samples maintain the NVPF structure with or without extra phases due to NVPF decomposition during leaching process.

Microscopic analyses on the leached samples:

To grasp further insights into those competing degradation-dissolution reactions, we relied on transmission electron microscopy (TEM) by focusing solely on the SL-NVPF and PF_6-NVPF

samples for which XRD could not identify the phases(s) present. HAADF-STEM images of the SL-NVPF crystals (supporting Fig. S8) shows numerous elongated pits and cracks confirming the leaching process. Moreover, STEM-EDX maps and EDX spectra (Fig. 5a, supporting Fig. S9) indicate a core-shell type structure with the sodium-rich core ($Na_{1.9(2)}$: $V_{1.999(8)}$: $P_{2.001(8)}$, as quantified from integrated EDX spectra) while the shell contains virtually no Na and F ($Na_{0.4(2)}$: $V_{2.00(1)}$: $P_{2.00(1)}$). A difference between the core and shell is also reflected with the EELS spectra (Fig. 5b) of the V-$L_{2,3}$ and O-K edges. In the EELS spectra from the core area there is a clear splitting of the V-L_3 and V-L_2 peaks indicative of coexisting V^{3+} (V-L_3 at ~518.1 eV) and V^{5+} (V-L_3 peak at ~519.6 eV) while the V-$L_{2,3}$ edge for the shell consists of two broad peaks centered at ~519.3 eV and 525.9 eV that is between the energy losses characteristic of V^{4+} and V^{5+}. It should be noted that the V cations in both core and shell are significantly more oxidized compared to vanadium in the pristine NVPF, which is in exclusively +3 oxidation state (Supporting Fig. S10).

The O-K edge EELS allows for differentiating the chemical nature of oxygen: the onset of a pre-peak at ~531 eV is related to the O2p−V3d hybridization representing "free" oxide ions (O^{2-} that are not bonded to the PO_4 group)[40] while the intense peak at 539.4 eV is due to mixed O2p and P3sp states (O^{2-} in the PO_4 group). The intense O2p−V3d pre-peak for the shell indicates that substantial amount of oxygen does not belong to the PO_4 groups. In contrast, the observed intensity of pre-peak at 531 eV is very low for the core in agreement with the $Na_{3-x}V_2(PO_4)_2F_3$ formula, taking into account that the spectrum from the core unavoidably includes the shell contribution. Combined with a low fluorine content, the chemical formula for the shell phase can be suggested as $Na_{0.4}V_2O_y(PO_4)_2F_z$. The presence of a vanadyl bond in the SL-NVPF was also confirmed by NMR and IR analyses (supporting Fig. S11). Thus, one can view the SL-NVPF sample as consisting of the core that is more reduced with high sodium content than the expected 1Na for 'charged NVPF' ($Na_{1.9}V_2(PO_4)_2F_3$) and the surface that is more oxidized, strongly desodiated, and richer in oxygen $Na_{0.4}V_2O_y(PO_4)_2F_z$.

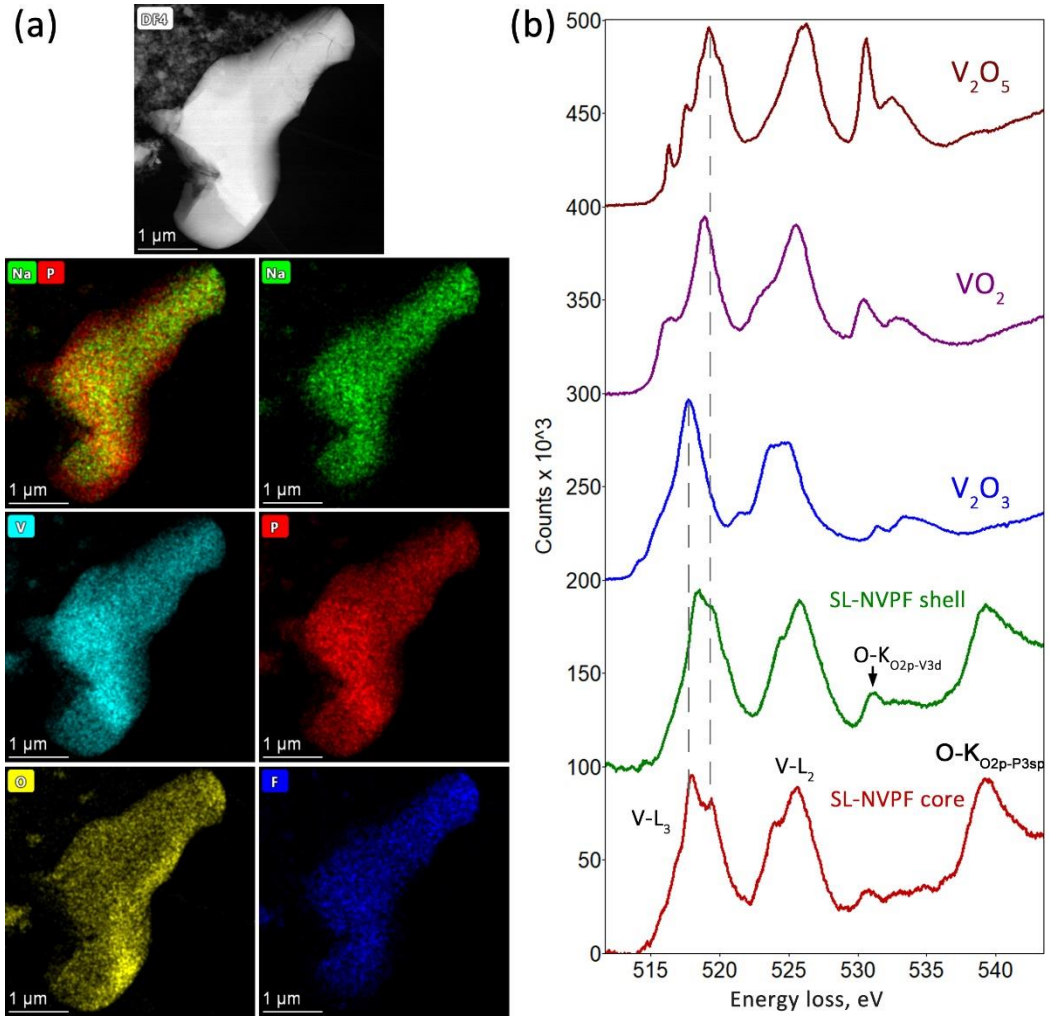

Fig. 5: **Identifying chemical changes in solvent-leached SL-NVPF using TEM.** (**a)** HAADF-STEM image with EDX compositional maps demonstrating Na-depleted core (looks red in the mixed Na/P map); (**b)** EELS spectra of the shell and core in SL-NVPF along with the characteristic spectra of vanadium oxides.

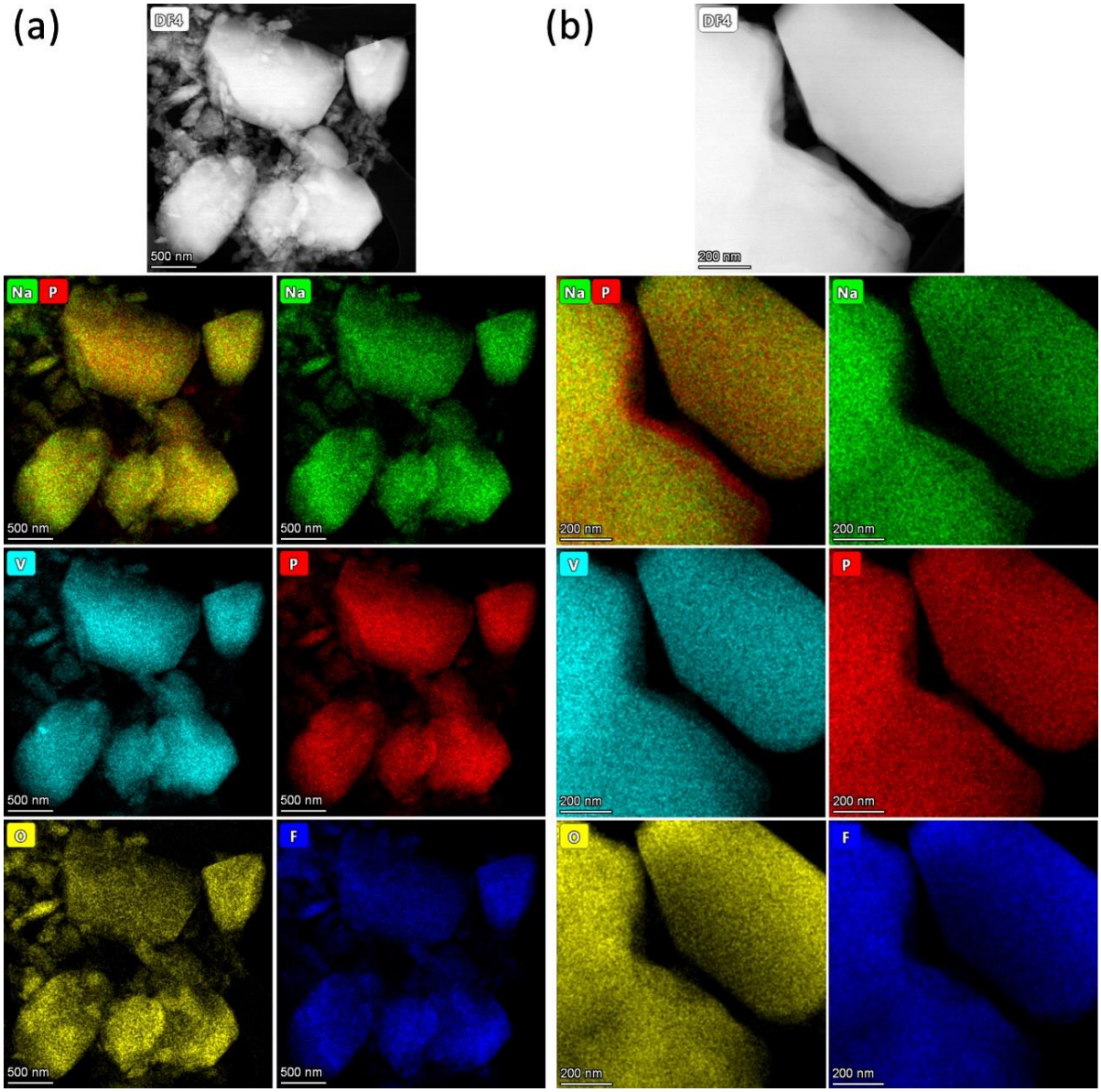

Fig. 6: **Identifying compositional changes in the electrolyte-leached NVPF using TEM.** (a) HAADF-STEM image and EDX compositional maps of the crystallites with different Na content visible in the mixed Na/P map due to different balance of green and red colors; (b) HAADF-STEM image and EDX compositional maps of the crystallite demonstrating a Na-depleted shell (looks red in the mixed Na/P map).

Turning to the crystallites of the PF_6-NVPF sample, they are largely disintegrated, forming numerous small loose, shapeless particles (Fig. 6a). EDX analyses on different particles show the presence of at least two different types (Fig. 6a, Supporting Fig. S12 a,b) exhibiting different sodium stoichiometry confined to the $Na_{1.7(3)}$: $V_{2.00(2)}$: $P_{2.00(2)}$ and $Na_{2.4(2)}$: $V_{2.00(1)}$: $P_{2.00(1)}$ formulas. Additionally, a core-shell type structure is observed (Fig. 6b) with the surface layer containing

almost no Na and significantly different V:P ≈ 1:2 ratio ($Na_{0.09(2)}$: $V_{1.00(2)}$: $P_{2.00(1)}$, Fig. S12c) indicating highly depleted vanadium regions. This suggests the feasibility of non-homogeneous vanadium dissolution in the PF_6-NVPF material. Moreover, the EELS spectra taken over the V-depleted shell regions (Supporting Fig. S13) demonstrate the V^{3+} signal exceeding that of V^{5+} indicating that the latter is leached predominantly.

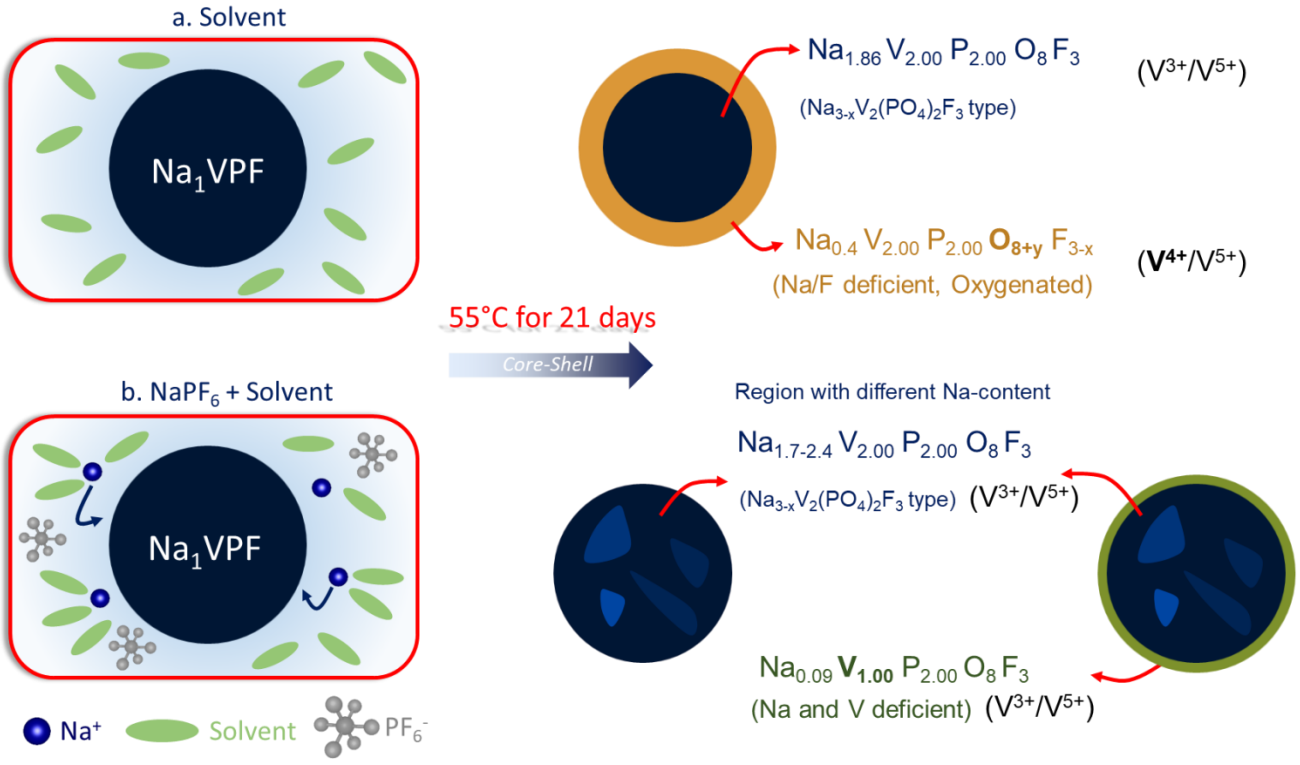

Fig. 7: **Schematic of structural degradation in SL- and PF_6-NVPF.** Structural changes undergone by Na_1VPF particle because of (**a)** Solvents leached NVPF leading to core-shell type structure with a thick shell containing oxygenated material. (**b)** Electrolyte (1M $NaPF_6$ in EC-PC-DMC) leached NVPF leading to core-shell type structure with a thin shell depleted in vanadium.

Overall, as depicted in Fig. 7, both SL- and PF_6- NVPF samples exhibit a core-shell type structure, with the core being richer in Na than in the starting phase Na_1VPF. In the presence of Na^+-free solvent, the observed Na excess in the SL-NVPF core can solely result from Na diffusion from surface to the core that is coherent with the Na-deficient surface/shell seen by TEM in this sample. This explains why the surface NVPF is more oxidized (contains V^{4+} and V^{5+}) than the core (V^{3+} and

V^{5+}) together with the observed capacity of ~50 mAh/g in the first charge (SL-NVPF Fig. 3a), owing to its Na-rich core. It is worth to note that the charge capacity for SL-NVPF is the lowest (in Fig. 3a) among the leached samples due to the Na^+ depleted from the surface in absence of Na^+ in the leaching media.

Nevertheless, a surprising observation with SL-NVPF is the presence of vanadyl (V=O) bond in the shell of the particles. The oxygen needed to form this V=O bond does not come from the solvent molecules since O-free solvent alike acetonitrile shows identical results (Supporting Fig. S14). Hence, we must suspect NVPF itself via a process that enlists the breaking of O-PO_3 bonds that release phosphate anions into the solvent to form vanadyl bond together with the sodium migration from surface to the bulk of NVPF. This explanation is substantiated by NMR studies that reveal the presence of phosphate anion in the recovered solvents from the leaching reaction leading to SL-NVPF. In contrast, no phosphate species were present in the ones recovered from the leaching reaction leading to PF_6-NVPF (supporting Fig. S15).

Altogether, we observed a different leaching mechanism associated to either solvent or $NaPF_6$ electrolyte. For SL-NVPF, the process is homogeneous with particles undergoing internal redox process leaving a V=O rich and Na-depleted shell. In the case of PF_6-NVPF, the leaching is not homogeneous, and leads to the formation of V-deficient shells, which account for the inactive phases observed before by XRD and electrochemical cycling.

Mechanism of the self-discharge-degradation process as a function of the solvent/ electrolyte media:

Based on the aforementioned observations we propose a reaction scheme (Fig. 8) to account for the formation of PF_6-NVPF, TFSI-NVPF, and SL-NVPF samples. In all cases, a self-discharge phenomenon is evidenced by the capacity recorded during the first charge after recovering the

materials (Fig. 3b). However, the reducing agent donating the required electrons to fuel the self-discharge process differs in each case, resulting in different reaction pathways, as we detailed below.

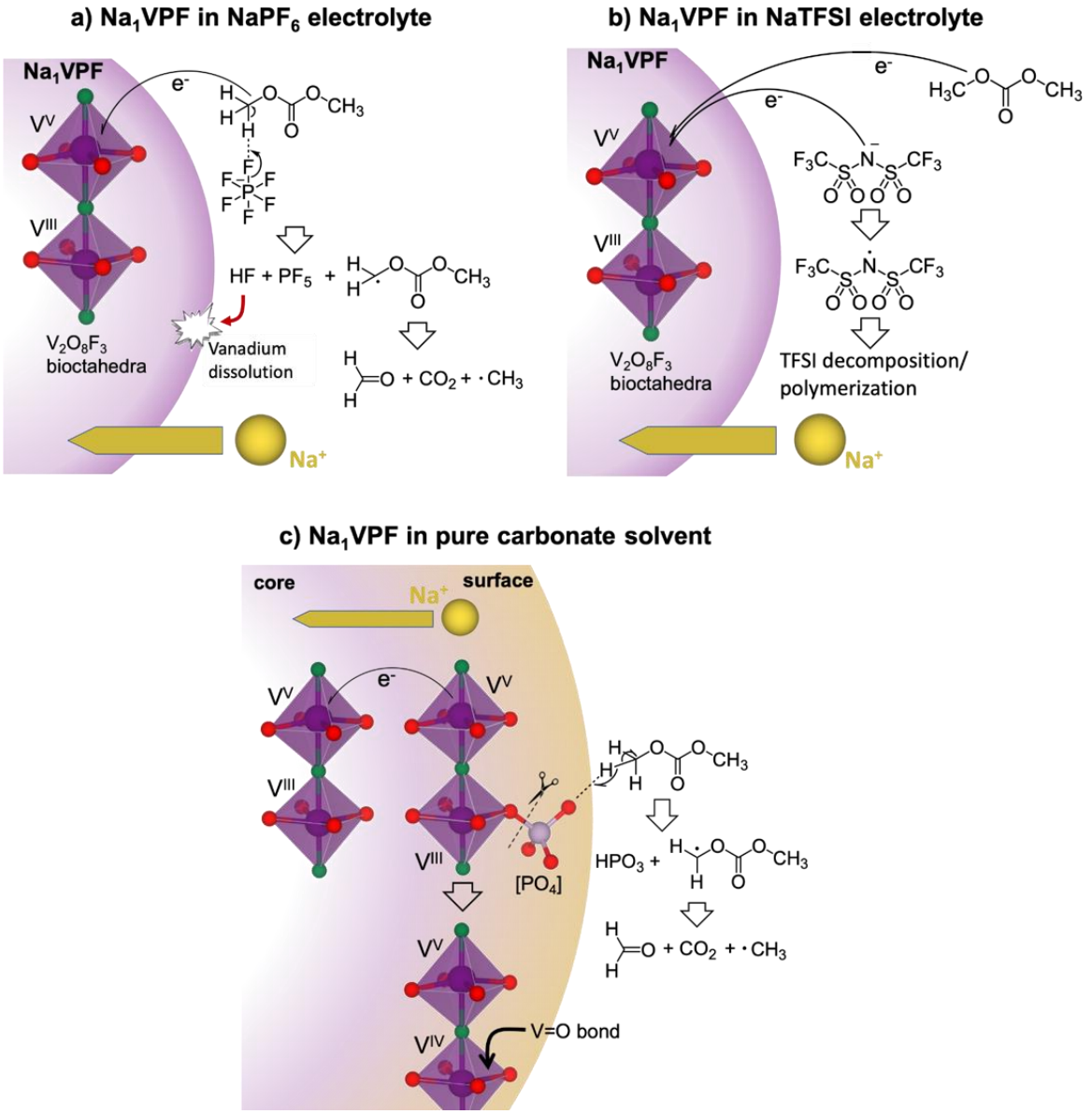

Fig. 8: **Mechanism representing structural degradation of Na_1VPF in $NaPF_6$, NaTFSI, and pure carbonate solvent.** (**a)** For $NaPF_6$ based electrolyte, simultaneous oxidation of DMC and Na^+ insertion in Na_1VPF with the formation of HF and its attack on Na_1VPF particle surface. (**b)** For NaTFSI based electrolyte, simultaneous Na^+ insertion in Na_1VPF particle and oxidation of $TFSI^-$ anion leading to TFSI decomposition. (**c)** The Na_1VPF –solvent interaction proceeds with internal phase separation in Na_1VPF with simultaneous solvent oxidation. Note that oxidation of DMC molecule is used here as a representative example, whereas, in reality EC and PC could also undergo similar oxidation pathways.

Firstly, in the presence of $NaPF_6$ electrolyte (Fig. 8a), Na^+ cations are inserted in Na_1VPF, while the carbonate solvent (EC/ PC/ DMC) is oxidized[41–44]. This oxidation is promoted by the interaction with PF_6^- anions[45], forming PF_5 and HF (confirmed by ^{19}F-NMR, supporting Fig. S16), the latter being responsible for the V-dissolution observed by ICP. Additionally, the organic radical formed after solvent dehydrogenation eventually decomposes into formaldehyde, CO_2, and a methyl radical that can attack other electrolyte components and generate CH_4 as supported by mass spectroscopy (Supporting Fig. S17 and table S2).

A different scenario is proposed with the NaTFSI electrolyte where the $TFSI^-$ anions get oxidized together with solvent[45], without the formation of HF (confirmed by NMR, supporting Fig. S18), thus avoiding the V-dissolution. The radical formed by the oxidation of $TFSI^-$ is stabilized by the high charge delocalization of the anion, although it can eventually decompose/polymerize with or without the evolution of gaseous by-products. The absence of HF release through this anion decomposition explains the barely detectable V-dissolution observed. Nevertheless, the charged NVPF in this electrolyte still shows large self-discharge, associated with electrolyte oxidation that we must address before using NaTFSI-based electrolytes for Na-ion cells.

Turning to the SL-NVPF sample, it shows the more pronounced structural changes associated to a reduction of the core of the particles with the surface acting as a reductant (See EELS data in Fig. 5b). This redox process affects the homogeneous distribution of V^{3+}-V^{5+} bi-octahedra in Na_1VPF material with the core evolving towards V^{3+}-V^{4+} (which eventually disproportionate back to V^{3+}-V^{5+}) while the surface changes into V^{4+}-V^{5+}. As V^{4+} is not stable in this coordination environment, the ligands must reorganize, producing some dissolution of either PO_3^- groups (^{31}P NMR of collected leached solvent shows the presence of P in solution) or F^- together with a small amount of vanadium. These findings lead to the proposed reaction scheme (Fig. 8c) to account for the formation of the vanadyl bonds (V=O) in the SL-NVPF material, while a more detailed reaction mechanism requires further *operando* experiments.

Implication of dissolved vanadium on the electrochemistry of NVPF-HC cells:

After having studied the structural and electrochemical modification suffered by the NVPF material due to some vanadium dissolution, we now turn our attention to the effect of such dissolved vanadium in the electrochemical reactivity of the electrolyte. As a first step, we analyzed the nature of vanadium present in the $NaPF_6$ based electrolyte after leaching process, termed hereafter as PF_6-leached electrolyte (see the ^{51}V-liquid NMR result in supporting Fig. 19). The absence of an NMR signal for PF_6-leached electrolyte indicates that vanadium is present in either +2, +3, or +4 oxidation states.

Next, the PF_6-leached electrolyte was tested by cyclic voltammetry using the glassy carbon and platinum mesh as working and counter electrodes respectively and an organic Ag^+/Ag reference electrode.[6,15] The anodic sweep shows an oxidation peak around 3.9 V vs. Na^+/Na^0 (Fig. 9a) and some reduction current is observed in the subsequent cathodic sweep although without a clear reduction peak. Upon further reduction to 1 V vs. Na^+/Na^0 (supporting Fig.20), the vanadium reduction process is observed at 1.36 V vs. Na^+/Na^0. The CV results show that the PF_6-leached electrolyte containing dissolved vanadium is redox-active and could undergo oxidation-reduction on NVPF and HC electrode surfaces, which operate at potentials between 3- 4.3 V and 2- 0.0 V vs. Na^+/Na^0, respectively, in a full NVFP-HC cell.

A similar CV experiment was carried out using the soluble vanadium compound recovered from 18650 cell after the CID break by washing the NVPF electrode with EC-PC-DMC (shown in Fig. 1b) and using the resultant solution for making the electrolyte (green electrolyte as mentioned in experimental section) by adding 1M $NaPF_6$. The anodic sweep between 2 to 4.3 V vs. Na^+/Na^0 in Fig. 9b indicates oxidation (3.34 V and 3.9 V) and reduction (3.2 and 3.6 V) processes that are most probably associated to the soluble vanadium species.

In light of this finding, one would expect upon cycling of a NVPF- HC full cell, the emergence of some redox activity features that should increase with the amount of dissolved vanadium. Fig. 9c shows the cycling profile of NVPF-HC 18650 Na-ion cells cycled at high temperatures, and remarkably there is appearance upon long cycling (30 cycles) of an oxidation event occurring in the similar potential range (3.9 V; see arrow) as observed via cyclic voltammetry. This feature is further emphasized in Fig. 9d by plotting the derivative dQ/dV which shows nicely the appearance of the oxidation peak at around 3.4 and 3.9 V, which is partly/ fully reversible on reduction with the appearance of reduction processes between 3 and 3.7 V. The peaks could be correlated with the redox reaction of dissolved vanadium on the NVPF electrode surface (by comparing with CV in Fig. 9a and Fig. 9b). Its slow evolution from cycle to cycle (supporting Figure S21) indicates increasing concentration of soluble vanadium in the electrolyte during cycling, in agreement with the findings by ICP-MS discussed before. Therefore, these redox peaks could be used as finger prints for following the amount of dissolved vanadium during cycling. Our cross experiments using the fresh NVPF-HC cell with the electrolyte containing dissolved vanadium re-confirm the observations of vanadium oxidation and the changes in the cycling profile due to dissolved vanadium (supporting Fig. S22).

At the same time, the dissolved vanadium can also be reduced in the negative electrode, as hard carbon spends most of its time at very low potentials (~0.05 V vs. $Na^{+/}Na^{0}$). If the vanadium reduction leads to its deposition on the HC surface, it could lead eventually to surface passivation, active material loss and impedance increase (note the polarization increase in the low voltage region of cycling in Fig. 9c). It is important to note here that the acidic impurities (HF, HPO_2F_2 etc.) formed during the electrolyte oxidation, as mentioned in previous reports[45–47], can also play a role in dissolution and recreation of interphases (SEI, CEI) leading to Na-inventory loss as well as increasing cell impedance. The influence of acidic impurities in the performance of NVPF | HC cells is a subject that requires deeper studies, which will be presented in future reports.

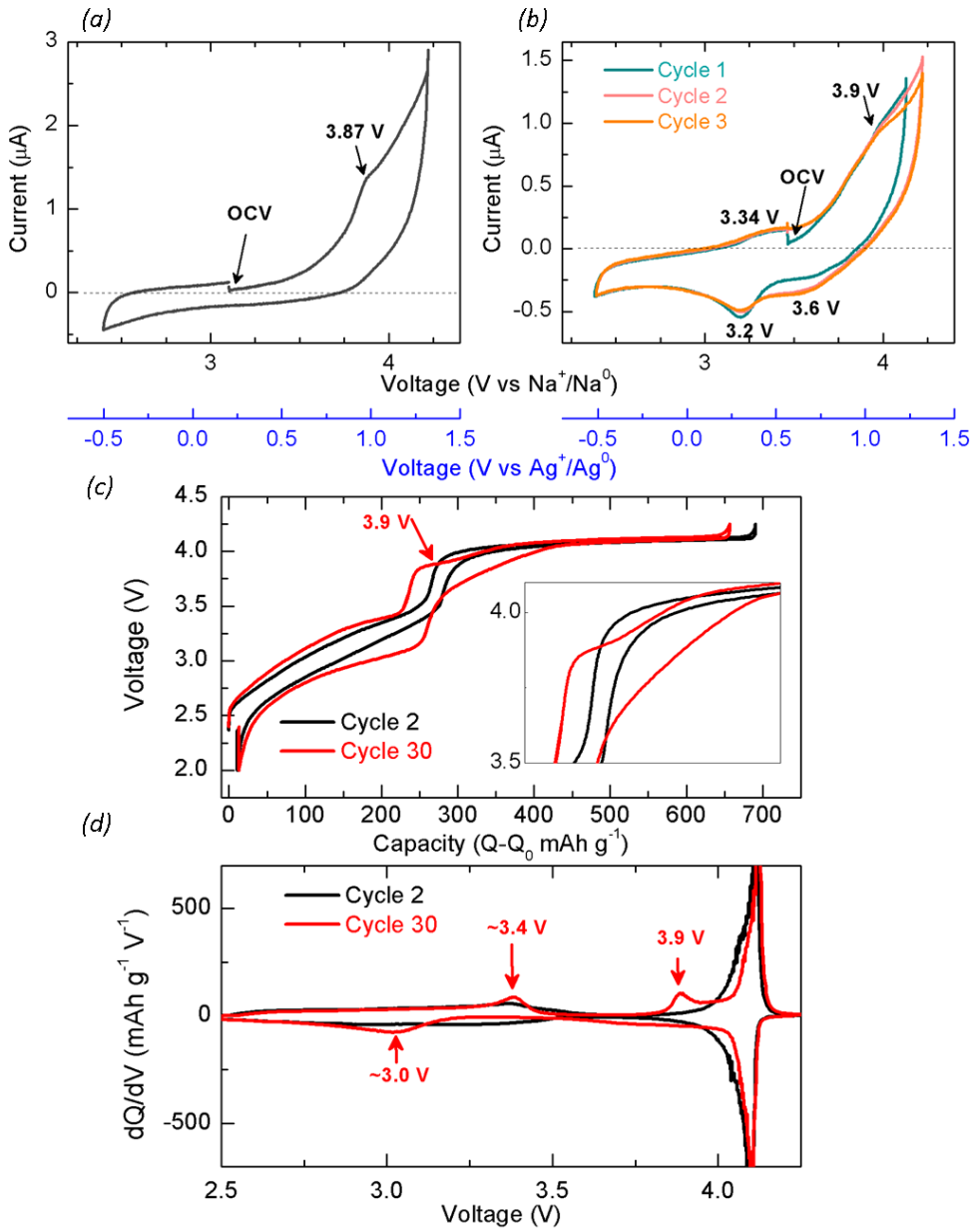

Fig. 9: **Effect of dissolved vanadium on NVPF-HC cell electrochemistry.** Three-electrode cyclic voltammetry of **(a)** $NaPF_6$ electrolyte recovered after NVPF leaching, cycled in the voltage window of 2.27-4.3 V vs. Na^+/Na^0 with scan rate of 20 mV/s. **(b)** CV of the electrolyte prepared by washing NVPF from 18650 with EC-PC-DMC (shown in Fig.1b) and then adding 1M $NaPF_6$ in 2.27-4.3V vs. Na^+/Na^0 with scan rate of 20 mV/s. **(c)** Electrochemical profile and (d) corresponding dQ/dV profile for 2nd and 30th cycle of NVPF-HC 18650 cell cycled at 55 °C with C/5 rate.

A consequence of the evolution of these redox processes and of the increased polarization in the low voltage region (2-3.6 V) was always concomitant with the pressure increase (e.g, CID break) of the 18650 cells, although we don't fully master the associated parasitic reactions yet. Meanwhile, it is

essential to reduce this V-dissolution from NVPF in order to improve the cell life of the NVPF-HC cells. Hence, we studied the following strategies to reduce and possibly eliminate V-dissolution completely.

Suppressing partially the vanadium dissolution problem:

As our first strategy, we explore using NaTFSI as the electrolyte salt, as it prevents the V-dissolution into the electrolyte (Fig. 2). However, NaTFSI solely as electrolyte salt corrodes the Al current collector at high potential[48], therefore a mixture of $NaPF_6$ and NaTFSI must be used. Fig. 10a compares the discharge capacity (%) at 55°C with 1M $NaPF_6$ and 0.7M $NaPF_6$ - 0.3M NaTFSI in 1:1:2 mixture of EC-PC-DMC. The cells are allowed to rest after 10 cycles at 100% SOC for 1 week to promote parasitic reactions. The capacity loss during self-discharge is almost similar in both cells (Fig. 10b). However, the capacity recovery in the subsequent cycle is higher (less irreversible capacity loss during self-discharge) with NaTFSI containing electrolyte. The capacity retention (Fig. 10a) after self-discharge is also higher for NaTFSI containing electrolyte with less changes in cell polarization (Fig. 10c) compared to a huge increase in cell resistance and poor capacity retention for the 1M $NaPF_6$ electrolyte. After 850 h of cycling, the cells were disassembled and the hard carbon electrode and one separator were analyzed for V-content by ICP. The ICP results in Fig. 10d show 5.45% vanadium dissolution for the cells containing 1M $NaPF_6$ electrolyte, whereas only 2.17% for the $NaPF_6$:NaTFSI mixed electrolyte. The results are encouraging, although we still observed self-discharge loss of 25% in both cells indicates some degree of electrolyte oxidation. This calls for further curing tricks that are being tried in our group at present.

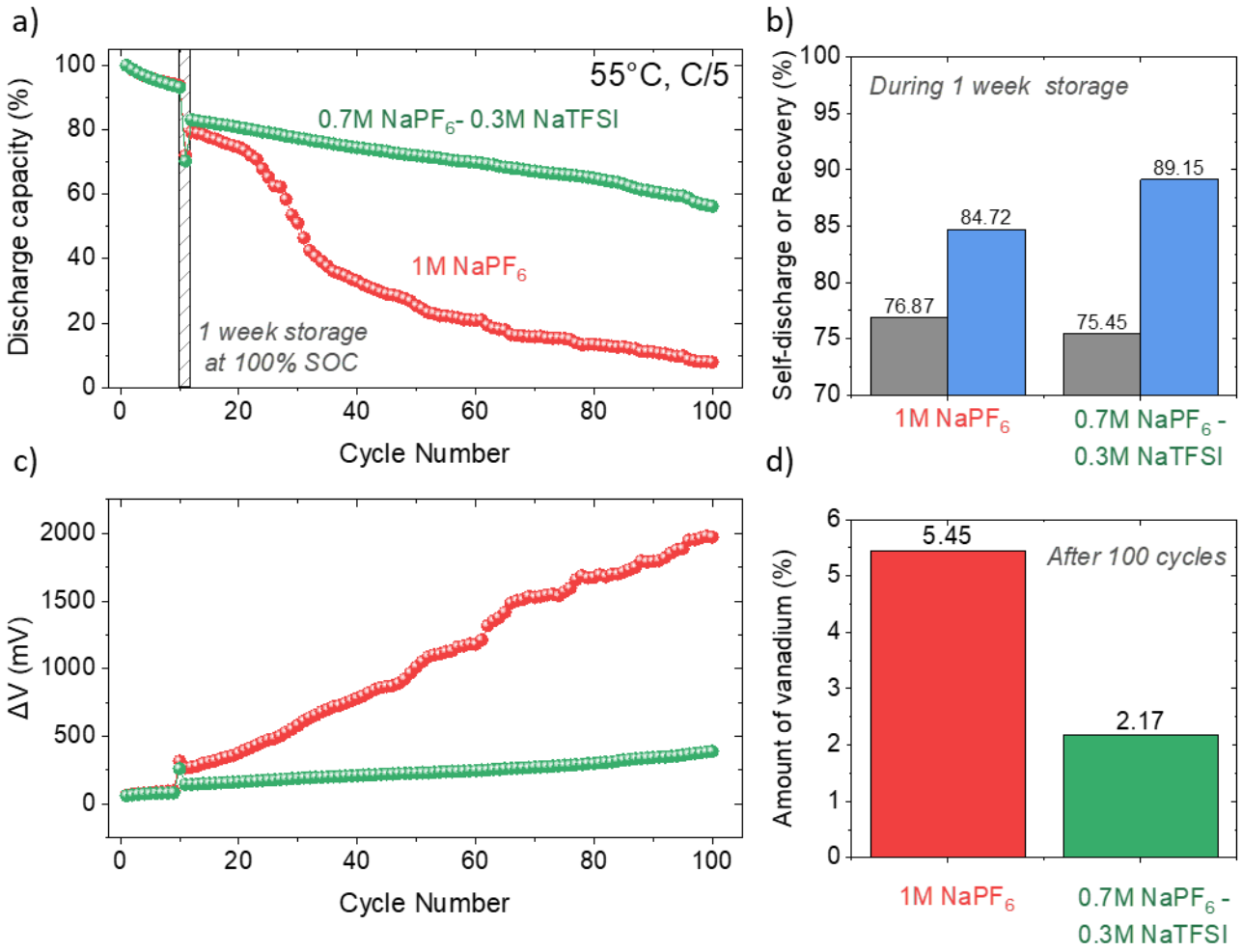

Fig. 10: **Effect of NaTFSI in protecting the NVPF surface.** 1M $NaPF_6$ or 0.7M $NaPF_6$-0.3M NaTFSI in EC-PC-DMC (1:1:2) was used as an electrolyte for NVPF-HC coin cells cycled at 55 °C at C/5 rate. (a) Discharge capacity retention. (b) self-discharge (Q_9/Q_{10}) and recovery(Q_{11}/Q_{10}) process during the storage period. (c) Polarization evolution (in terms of ΔV= average charge voltage – average discharge voltage). (d) Amount of vanadium in the coin cells after 100 cycles measured with ICP-MS.

Meanwhile, in the second approach, we tested solely $NaPF_6$ as electrolyte salt and introduced electrolyte additives that protect the NVPF surface. To do so we used the electrolyte formulation reported in our previous work that consists of 1M $NaPF_6$ in an EC-PC-DMC mixture with 4 additives, namely NaODFB, VC, SN, and TMSPi. Fig. 11 a shows that the amount of dissolved vanadium after 1 week storage of NVPF-HC coin cells at 55 °C in 100 % SOC is reduced by nearly 50 % in presence of additives. Encouraged by these results, 18650 cylindrical cells loaded with this

electrolyte were cycled. They exhibit over four months of tests (Fig. 11b) at 55 °C a better capacity retention without any CID break, in comparison to the cells without any electrolyte additive that dies just after 10 days (same cell as used in Fig. 1). This confirms the beneficial effect of the electrolyte additives. Interestingly, the derivative plot shows upon cycling the appearance of a barely noticeable 3.9 V peak (arrow Fig. 11c left) for the electrolyte containing additives as opposed to a well pronounced feature for the electrolyte without additives. Bearing in mind that this peak is the fingerprint of V-dissolution, these results unambiguously confirm the positive attribute of using electrolyte additives to reduce vanadium dissolution and improves the cycling performance at high temperature, but not to fully eliminate it.

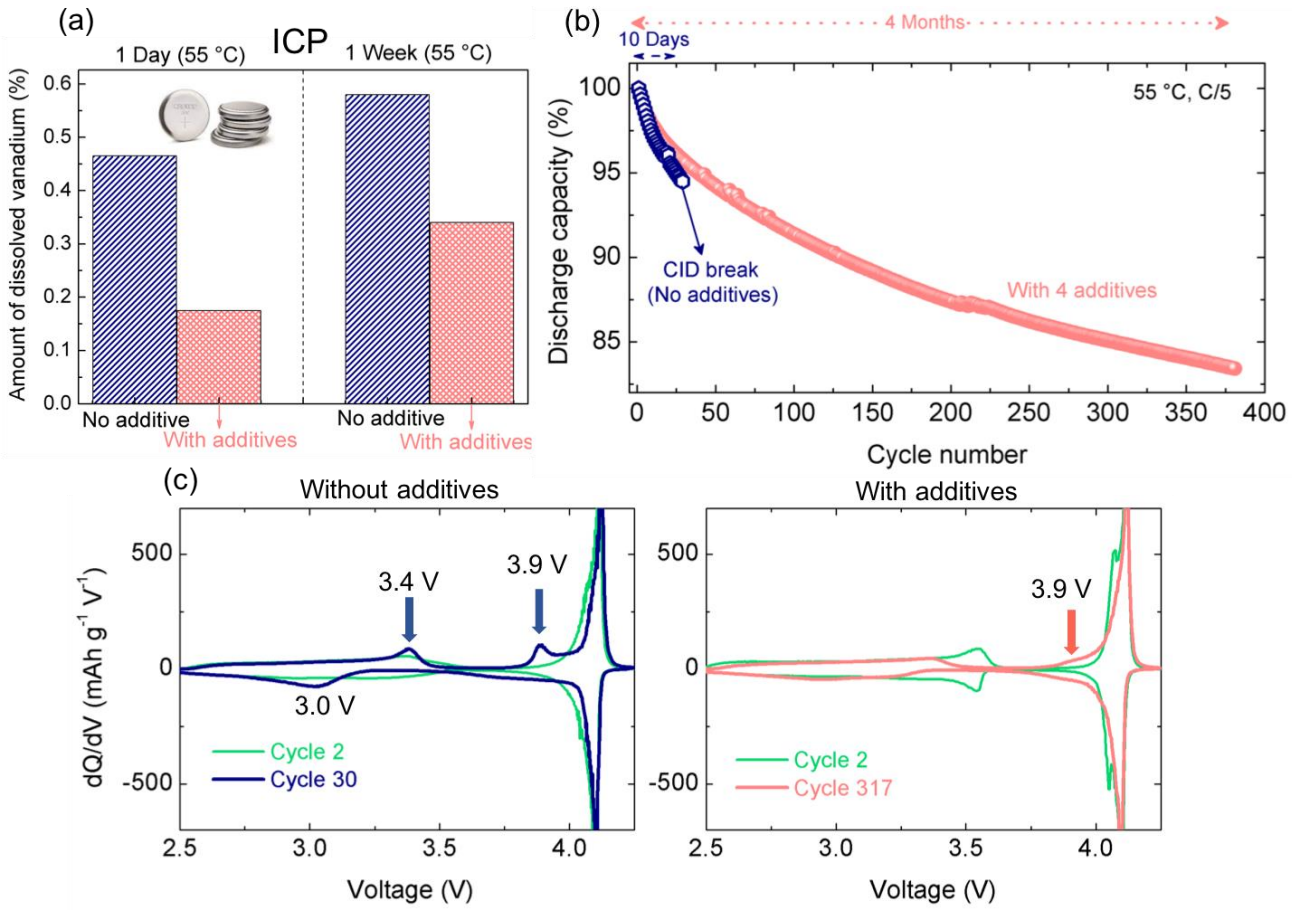

Fig. 11: **Effect of electrolyte additives in protecting the NVPF surface. a.** ICP analyses on hard carbon+ 1 separator recovered from the cells cycled using 1M $NaPF_6$ in EC-PC-DMC with and without electrolyte additives. The cells were stored at 100 % SOC, for one week at 55°C before decrimping to do ICP analyses. (b) Percentage capacity retention of

the 18650 cell used in Figure 1 (blue diamond points) in comparison to another 18650 cell from the same batch of electrodes, however with electrolyte containing 4 additives namely 0.5 % NaODFB, 3 % VC, 3 % SN and 0.5 % TMSPi (red circles). The cells were cycled at 55 °C at C/5 rate. (c) The comparison of derivative plots of the two cells where the second and last cycles were compared. The appearance of new redox process around 3.9 V is not very evident for the cells having electrolyte with additives even after 4 months of cycling at 55 °C, in comparison to 10 days cycling of the cell without electrolyte additive.

The third strategy has consisted in exploring the coating of NVPF particles by preparing two batches of NVPF having different amounts of carbon coating as determined by TGA analyses (Fig. 12a). Batches 1 and 2 show carbons contents of ~7% and ~3%, respectively, with a more uniform C-coating for batch 1 as deduced from EDX mapping (supporting Fig. S23). Both batches were then tested for vanadium dissolution in coin cells (1M $NaPF_6$ in EC-PC-DMC as electrolyte) by storing them at 100 % SOC for one week at 55 °C, and the results in Fig.12b show a higher amount of vanadium dissolution for the NVPF sample having the lowest amount of coated C (Batch2). Moreover, coin cells using both batches as the positive electrode and additive-free electrolyte were cycled at 55 °C. Their capacity retention and polarization evolution upon cycling, Fig. 12 c and 12d, respectively, show that NVPF with higher (7%) carbon coating presents less self-discharge loss during rest (1 week) together with a lower polarization after the self-discharge process, when compared to the NVPF having solely 3 % C-coating. Altogether, the results confirm the positive attributes of carbon coating towards reducing vanadium dissolution during rest at 100 % SOC.

To ensure the robustness of this C-coating effect we compared (Fig. 12e) the capacity retention plots at 55 °C of 18650 Na-ion cells, comprising NVPF positive electrode with 3 and 7% carbon coating, hard carbon negative electrode and 1M $NaPF_6$ in EC-PC-DMC with 4 additives (NaODFB, VC, SN and TMSPi) as the electrolyte. Though the capacity retentions are nearly similar for both cells, the one containing 7% C coated NVPF displays slightly higher efficiency indicative of less parasitic reactions than the cell containing 3% C coated NVPF. The derivative plot in Fig. 12f further supports

the above trend since a lower evolution of the redox process at ~3.9 V (the fingerprint region as explained in Figure 9) and ~3.2 V for NVPF is observed for the higher carbon content (green plots Fig. 12f) indicative of a lower vanadium dissolution for the 7% C coated sample.

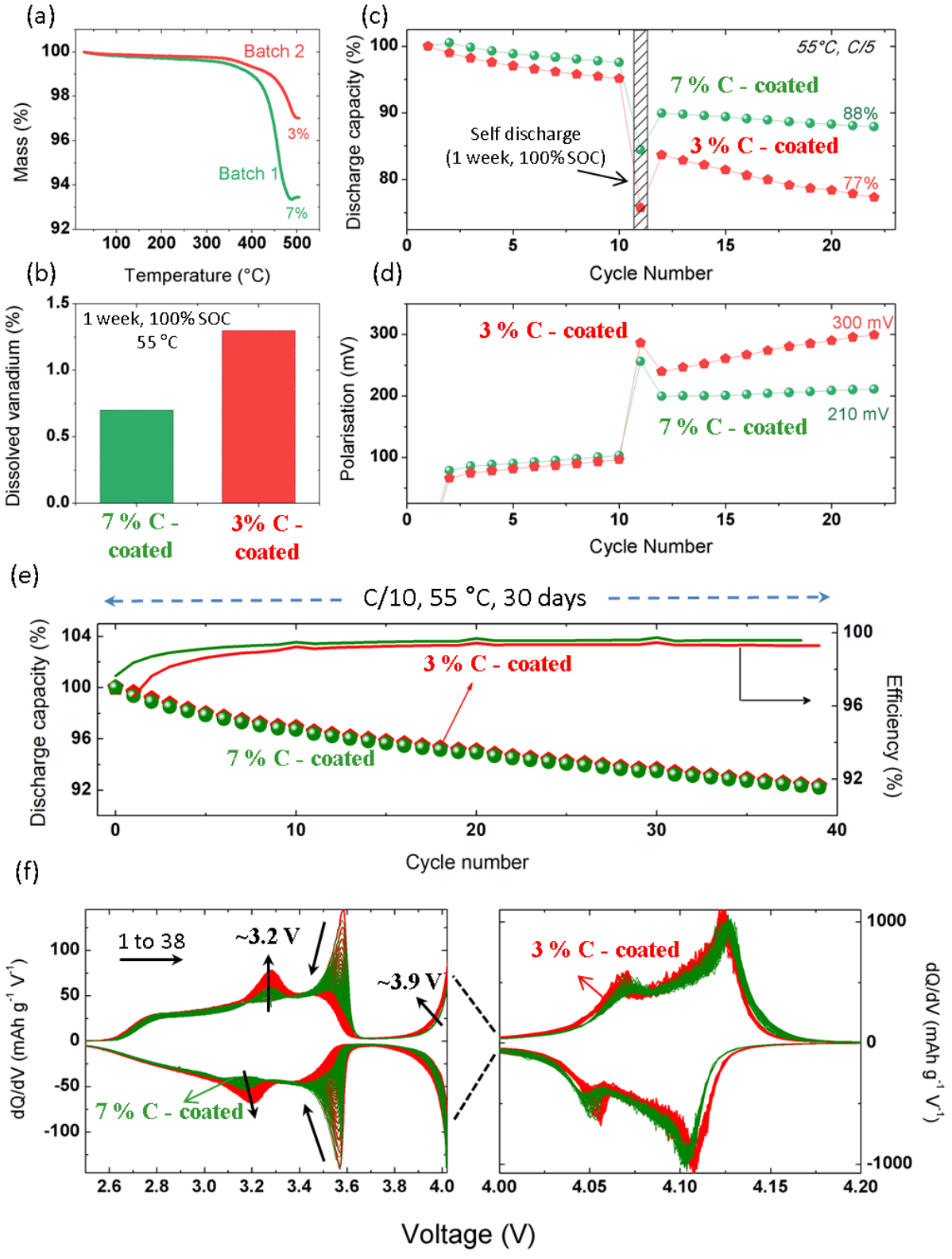

Fig. 12: **Effect of carbon coating on vanadium dissolution and cell electrochemistry. a.** TGA analysis of Batch-1 and Batch-2 for amount of carbon coating. **b.** Amount of vanadium dissolved from NVPF for 7 and 3% C-coated NVPF when NVPF-HC cell was stored at 55 °C for 1 week. **c.** Discharge capacity retention of 7 and 3% C-coated NVPF in NVPF-HC full cell mode at 55 °C with C/5 rate. **d.** Corresponding cell polarization in terms of ΔV= (average charge voltage – average discharge voltage) **e.** Discharge capacity retention for commercial 18650 type NVPF-HC cell containing 7 and 3% C-coated NVPF with the 1M $NaPF_6$ in EC-PC-DMC and VC + NaODFB + SN + TMSPi additives. **f.** Corresponding dQ/dV profile of 18650 cells with the arrows indicating the changes in the curve. Note that the hard carbon used and the positive to negative electrode materials balancing between the 18650 cells used in Fig. 11 and in Fig. 12 are slightly different, hence the observed difference in the cycling profile and corresponding derivative plots.

In short, combining the positive effect of additives and carbon coating of NVPF helps reducing the NVPF-electrolyte interface reactivity. However, a negative side effect of increasing the carbon content (e.g, thickening of the coating) is a decrease of the material specific energy and possibly the power rate capability. Thus, proper tuning of surface coating together with a careful choice of electrolyte formulation combined with the establishment of an optimized formation cycle is crucial to minimize the extent of V-dissolution and, therefore, to obtain, at the industrial-level, high performing NVPF/HC Na-ion cells.

Conclusion:

Transition metal dissolution is a significant problem for various battery chemistries and is not fully resolved for even matured Li-ion battery technology after 25 years of research. In this study, we provide evidence that 3d metal dissolution is equally a severe problem for sodium-ion batteries and more so for the NVPF/HC chemistry since the redox potential of NVPF (~4.2 V vs. Na/Na^+) falls beyond the thermodynamic stability of the electrolytes. Vanadium from charged NVPF dissolves at high temperature in conventional electrolytes. This dissolved vanadium is redox active and can trigger redox shuttle reactions in both positive and negative electrodes, thereby deteriorating the

electrochemical performance of the cell. Suppressing vanadium dissolution is an essential step to improve the cycle life and slow down cell aging.

In this study we report on our efforts to prevent the V-dissolution in NVPF|HC cells. First, we show that a NaTFSI-based electrolyte prevents this process to happen, but still undergo degradation at high potentials. Therefore, a better strategy must be designed to avoid NaTFSI oxidation and protect the aluminum current collector on high voltage cycling of NVPF-HC cells. Second, we demonstrated that another attractive strategy to reduce vanadium dissolution is rooted in the coating of NVPF particles by carbon and surface protection using electrolyte additives. Overall, we show the importance of mastering the synergy between electrode and electrolyte to reach the best optimum performance of the NVPF/HC Na-ion cells.

Technology-wise, the gained knowledge from this work will further help in tuning the cell chemistry and engineering as well as formation protocol to reduce/eliminate the vanadium dissolution, hence fasten the commercialization of NVPF-HC based Na-ion cells. From a fundamental point of view, we believe the study provides a key understanding of how transition metal dissolution happens, its relation with the different salts, and the role of dissolved transition metal in altering the electrochemical performance of the cell. Similar studies could be extended to any new chemistry to pave the way to improve the system-level performance from fundamental understanding.

Acknowledgments:

The authors thank the RS2E Network for funding as well as the financial support of Région Nouvelle Aquitaine, of the French National Research Agency (STORE-EX Labex Project ANR-10-LABX-76-01). S. M. acknowledges Horizon 2020 research and innovation program under grant agreement No 875629- NAIMA. P. D. thanks RS2E for PhD funding. TIAMAT, France is gratefully acknowledged for providing the NVPF/HC 18650 cells specifically designed for R&D purposes as well as the NVPF, HC electrodes for the coin cell studies. Use of the 11-BM mail-in service of the APS at

Argonne National Laboratory was supported by the US Department of Energy under contract No. DE-AC02-06CH11357 and is gratefully acknowledged. Access to TEM facilities was granted by the Advance Imaging Core Facility of Skoltech. The authors acknowledge Damien DEGOULANGE (Collège de France) for the help with mass spectrometry analyses.

Conflict of interest

The authors declare no conflict of interest.

Associated Content

*Supporting Information

The Supporting Information containing additional cycling, XRD, NMR, IR and TEM images is available.

Reference:

1 Lithium mining, https://www.volkswagenag.com/en/news/stories/2020/03/lithium-mining-what-you-should-know-about-the-contentious-issue.html, (accessed June 8, 2021).
2 Y. Tian, G. Zeng, A. Rutt, T. Shi, H. Kim, J. Wang, J. Koettgen, Y. Sun, B. Ouyang, T. Chen, Z. Lun, Z. Rong, K. Persson and G. Ceder, *Chem. Rev.*, 2021, **121**, 1623–1669.
3 F. Duffner, N. Kronemeyer, J. Tübke, J. Leker, M. Winter and R. Schmuch, *Nat Energy*, 2021, **6**, 123–134.
4 R. Usiskin, Y. Lu, J. Popovic, M. Law, P. Balaya, Y.-S. Hu and J. Maier, *Nat Rev Mater*, 2021, **6**, 1020–1035.
5 C. Vaalma, D. Buchholz, M. Weil and S. Passerini, *Nat Rev Mater*, 2018, **3**, 18013.
6 H. Hijazi, P. Desai and S. Mariyappan, *Batteries & Supercaps*, 2021, **4**, 881–896.
7 J.-M. Tarascon, *Joule*, 2020, **4**, 1616–1620.
8 P. Desai, J. Huang, H. Hijazi, L. Zhang, S. Mariyappan and J. Tarascon, *Adv. Energy Mater.*, 2021, 2101490.
9 R. Mogensen, S. Colbin and R. Younesi, *Batteries & Supercaps*, 2021, **4**, 791–814.
10 A. Rudola, A. J. R. Rennie, R. Heap, S. S. Meysami, A. Lowbridge, F. Mazzali, R. Sayers, C. J. Wright and J. Barker, *J. Mater. Chem. A*, 2021, **9**, 8279–8302.
11 J.-M. Le Meins, M.-P. Crosnier-Lopez, A. Hemon-Ribaud and G. Courbion, *Journal of Solid State Chemistry*, 1999, **148**, 260–277.
12 M. Bianchini, N. Brisset, F. Fauth, F. Weill, E. Elkaim, E. Suard, C. Masquelier and L. Croguennec, *Chem. Mater.*, 2014, **26**, 4238–4247.
13 T. Broux, F. Fauth, N. Hall, Y. Chatillon, M. Bianchini, T. Bamine, J. Leriche, E. Suard, D. Carlier, Y. Reynier, L. Simonin, C. Masquelier and L. Croguennec, *Small Methods*, 2019, **3**, 1800215.

14 G. Yan, K. Reeves, D. Foix, Z. Li, C. Cometto, S. Mariyappan, M. Salanne and J.-M. Tarascon, *Advanced Energy Materials*, 2019, **9**, 1901431.
15 C. Cometto, G. Yan, S. Mariyappan and J.-M. Tarascon, *J. Electrochem. Soc.*, 2019, **166**, A3723–A3730.
16 P. Desai, J. Abou-Rjeily, J.-M. Tarascon and S. Mariyappan, *Electrochimica Acta*, 2022, **416**, 140217.
17 G. Amatucci, A. Du Pasquier, A. Blyr, T. Zheng and J.-M. Tarascon, *Electrochimica Acta*, 1999, **45**, 255–271.
18 A. Blyr, A. Du Pasquier, G. Amatucci and J.-M. Tarascon, *Ionics*, 1997, **3**, 321–331.
19 G. G. Amatucci, C. N. Schmutz, A. Blyr, C. Sigala, A. S. Gozdz, D. Larcher and J. M. Tarascon, *Journal of Power Sources*, 1997, **69**, 11–25.
20 V. Meunier, M. L. D. Souza, M. Morcrette and A. Grimaud, *J. Electrochem. Soc.*, 2022, **169**, 070506.
21 C. Zhan, T. Wu, J. Lu and K. Amine, *Energy Environ. Sci.*, 2018, **11**, 243–257.
22 Y. K. Lee, J. Park and W. Lu, *J. Electrochem. Soc.*, 2017, **164**, A2812.
23 Y. You, S. Xin, H. Y. Asl, W. Li, P.-F. Wang, Y.-G. Guo and A. Manthiram, *Chem*, 2018, **4**, 2124–2139.
24 J.-Y. Hwang, S.-T. Myung and Y.-K. Sun, *J. Phys. Chem. C*, 2018, **122**, 13500–13507.
25 H. Che, X. Yang, H. Wang, X.-Z. Liao, S. S. Zhang, C. Wang and Z.-F. Ma, *Journal of Power Sources*, 2018, **407**, 173–179.
26 L. Mu, X. Feng, R. Kou, Y. Zhang, H. Guo, C. Tian, C.-J. Sun, X.-W. Du, D. Nordlund, H. L. Xin and F. Lin, *Advanced Energy Materials*, 2018, **8**, 1801975.
27 J. Rodríguez-Carvajal, *Physica B: Condensed Matter*, 1993, **192**, 55–69.
28 K. Amine, J. Liu and I. Belharouak, *Electrochemistry Communications*, 2005, **7**, 669–673.
29 E. R. Logan, H. Hebecker, A. Eldesoky, A. Luscombe, M. B. Johnson and J. R. Dahn, *J. Electrochem. Soc.*, 2020, **167**, 130543.
30 A. Eldesoky, E. R. Logan, M. B. Johnson, C. R. M. McFarlane and J. R. Dahn, *J. Electrochem. Soc.*, 2020, **167**, 130539.
31 M. Koltypin, D. Aurbach, L. Nazar and B. Ellis, *Electrochem. Solid-State Lett.*, 2006, **10**, A40.
32 M. Dahbi, F. Ghamouss, F. Tran-Van, D. Lemordant and M. Anouti, *Journal of Power Sources*, 2011, **196**, 9743–9750.
33 A. M. Andersson, M. Herstedt, A. G. Bishop and K. Edström, *Electrochimica Acta*, 2002, **47**, 1885–1898.
34 J. T. Dudley, D. P. Wilkinson, G. Thomas, R. LeVae, S. Woo, H. Blom, C. Horvath, M. W. Juzkow, B. Denis, P. Juric, P. Aghakian and J. R. Dahn, *Journal of Power Sources*, 1991, **35**, 59–82.
35 M. Koltypin, D. Aurbach, L. Nazar and B. Ellis, 5.
36 A. Blyr, A. D. Pasquier and G. Amatucci, 1997, 11.
37 M. Metzger, P. Walke, S. Solchenbach, G. Salitra, D. Aurbach and H. A. Gasteiger, *J. Electrochem. Soc.*, 2020, **167**, 160522.
38 T. Broux, T. Bamine, F. Fauth, L. Simonelli, W. Olszewski, C. Marini, M. Ménétrier, D. Carlier, C. Masquelier and L. Croguennec, *Chem. Mater.*, 2016, **28**, 7683–7692.
39 M. Bianchini, F. Fauth, N. Brisset, F. Weill, E. Suard, C. Masquelier and L. Croguennec, *Chem. Mater.*, 2015, **27**, 3009–3020.
40 D. Burova, I. Shakhova, P. Morozova, A. Iarchuk, O. A. Drozhzhin, M. G. Rozova, S. Praneetha, V. Murugan, J.-M. Tarascon and A. M. Abakumov, *RSC Adv.*, 2019, **9**, 19429–19440.
41 D. S. Hall, A. Eldesoky, E. R. Logan, E. M. Tonita, X. Ma and J. R. Dahn, *J. Electrochem. Soc.*, 2018, **165**, A2365–A2373.
42 A. Ponrouch, E. Marchante, M. Courty, J.-M. Tarascon and M. R. Palacín, *Energy Environ. Sci.*, 2012, **5**, 8572.

43 O. Borodin, W. Behl and T. R. Jow, *J. Phys. Chem. C*, 2013, **117**, 8661–8682.
44 E. Björklund, M. Göttlinger, K. Edström, D. Brandell and R. Younesi, *ChemElectroChem*, 2019, **6**, 3429–3436.
45 K. Xu, *Chem. Rev.*, 2004, **104**, 4303–4418.
46 C. Jayawardana, N. Rodrigo, B. Parimalam and B. L. Lucht, *ACS Energy Lett.*, 2021, **6**, 3788–3792.
47 S. K. Heiskanen, J. Kim and B. L. Lucht, *Joule*, 2019, **3**, 2322–2333.
48 B. Garcia and M. Armand, *Journal of Power Sources*, 2004, **132**, 206–208.